Tectonophysics 878 (2024) 230303

Contents lists available at ScienceDirect

Tectonophysics

journal homepage: www.elsevier.com/locate/tecto

Cretaceous extensional and contractional stages in the Colombian Andes unraveled by a source-to-sink geochronological and thermochronological study in the Upper Magdalena Basin

L. Calderon-Diaz [a], S. Zapata [b,*], A. Cardona [c], M. Parra [d], E.R. Sobel [e], A.M. Patiño [d], V. Valencia [f], J.S. Jaramillo-Rios [a,g], J. Glodny [h]

[a] Grupo de Estudios en Geología y Geofísica (EGEO), Departamento de Materiales y Minerales, Facultad de Minas, Universidad Nacional de Colombia, Medellín
[b] Grupo de Estudios en Geología y Geofísica (EGEO), Facultad de Ciencias Naturales, Universidad del Rosario, Bogotá, Colombia
[c] Grupo de Estudios en Geología y Geofísica (EGEO), Departamento de Procesos y Energía, Facultad de Minas, Universidad Nacional de Colombia, Medellín, Colombia
[d] Instituto de Geociências, Universidade de São Paulo, São Paulo, Brazil
[e] Institute of Geosciences, University of Potsdam, Potsdam, Germany
[f] School of Earth and Environmental Sciences, Washington State University, Pullman, USA
[g] Group of Studies in Orogenic Systems (GROSSE), Facultad de Minas, Universidad Nacional de Colombia, Medellín, Colombia
[h] GFZ German Research Centre for Geosciences, Potsdam, Germany

ARTICLE INFO

Keywords:
Source-to-sink
Northern Andes
Thermochronology
Sedimentary provenance
Extensional and broken foreland basins

ABSTRACT

Extensional and flexural basins can evolve through multiple stages under the same plate tectonic regime over tens of millions of years. The Cretaceous tectonic evolution of the Colombian Andes is characterized by shifts between contractional and extensional tectonics. The upper plate response to these changes is recorded in the Cretaceous sedimentary rocks along the Western, Central, and Eastern cordilleras, and their adjacent basins, including the Upper Magdalena hinterland basin. We integrated field observations, petrography, geochronology, and thermochronology in the Cretaceous sedimentary units in the southern Upper Magdalena Basin and in the adjacent crystalline basement to decipher the provenance of these units and the exhumation patterns of the source areas. These results suggest that the source areas were exhumed between the Late Jurassic to Early Cretaceous, which may have resulted from the combination of Jurassic contraction and the Early Cretaceous extension. Between ~120 and 100 Ma, a major stage of crustal extension is recorded in the Caballos Formation. Subsequently, between ~100 and 80 Ma, sedimentation in the Villeta Group marks the end of the extension and the onset of contraction. This contractional phase was characterized by minor rock uplift within the basin. Basin modification continued between 80 and 65 Ma, involving two successive contractional stages that changed the sedimentary patterns, leading to the burial of a previously exhumed horst block and the appearance of new source areas. These major changes in source areas and sedimentary systems are the result of deformation episodes during prolonged extensional and contractional phases. This geologic evolution highlights the stages that characterize extensional to contractional settings.

1. Introduction

Contractional and extensional tectonics along convergent margins can be long-lived processes that include different evolutionary stages that modify the sedimentary patterns, basin geometry, source areas, and paleogeography (e.g. Brune et al., 2023; DeCelles et al., 2011; DeCelles et al., 2009; Heermance et al., 2008). For instance, extensional tectonics includes various stages of doming and crustal stretching that control the development of sedimentary basins and the distribution of heat flow (Brune et al., 2023, Brune et al., 2017; Phillips et al., 2019; Scisciani et al., 2019). Similarly, contractional settings are characterized by the episodic or progressive development of one or several orogenic wedges, resulting in flexural subsidence and the associated foreland sedimentation or the reactivation of isolated inland structures that involve the older basement (DeCelles et al., 2011; DeCelles and Giles, 1996; Pfiffner, 2017; Roure, 2008; Siks and Horton, 2011).

* Corresponding author.
E-mail address: sebastian.zapatah@urosario.edu.co (S. Zapata).

https://doi.org/10.1016/j.tecto.2024.230303
Received 25 September 2023; Received in revised form 29 March 2024; Accepted 30 March 2024
Available online 3 April 2024
0040-1951/© 2024 The Authors. Published by Elsevier B.V. This is an open access article under the CC BY-NC-ND license (http://creativecommons.org/licenses/by-nc-nd/4.0/).

Erosion and deformation can obscure the tectonic evolution of source areas and associated sedimentary basins. However, source-to-sink studies that integrate multiple techniques such as petrography, and detrital and bedrock zircon geochronology and thermochronology can be used to unravel provenance signatures and basement unroofing histories providing insight into the different stages that characterized the long-term evolution of orogens (e.g. Bernet et al., 2009; Caracciolo, 2020; Chen et al., 2021; Coffey et al., 2019; Dong et al., 2011; Garzanti, 2016; Girault et al., 2023; Horton et al., 2015; Horton et al., 2010; Li et al., 2022; Malusà and Fitzgerald, 2019; Mora et al., 2020; Parra et al., 2020; Stojadinovic et al., 2017; Zapata et al., 2020).

The Northern Andes have been interpreted as an orogen characterized by long-lived (>30 Ma) extensional and contractional tectonic regimes, which have been controlled by changes in the subduction angle, the rate and direction of plate convergence, and the collision of exotic terranes against the continental margin (Cooper et al., 1995; Horton, 2018; Parra et al., 2012; Spikings et al., 2015; Siravo et al., 2019). During the Early Cretaceous (145–100 Ma), the Northern Andes were characterized by extensional settings responsible for the development of several intra-arc and back-arc basins that were inverted during the subsequent contractional phases (Sarmiento-Rojas et al., 2006; Spikings et al., 2015; Zapata et al., 2019a). These contractional events include the onset of the Andean orogeny and the collision of the Caribbean plateau between 72 and 60 Ma (Bayona et al., 2012; Cardona et al., 2020; Cardona et al., 2012; George et al., 2021; Horton et al., 2015; Horton et al., 2010; Montes et al., 2019; Mora et al., 2020; Mora et al., 2013; Mora et al., 2006; Parra et al., 2012; Parra et al., 2009; Spikings et al., 2015; Zapata et al., 2019a).

Although a regional temporal framework for these long-lived extensional and contractional settings has been reasonably constrained (Bayona, 2018; Cardona et al., 2020; Carvajal-Torres et al., 2022; Montes et al., 2019; Sarmiento-Rojas, 2019; Sarmiento-Rojas et al., 2006; Spikings et al., 2015; Zapata et al., 2019a, 2020), a detailed spatiotemporal reconstruction of the tectonic processes that

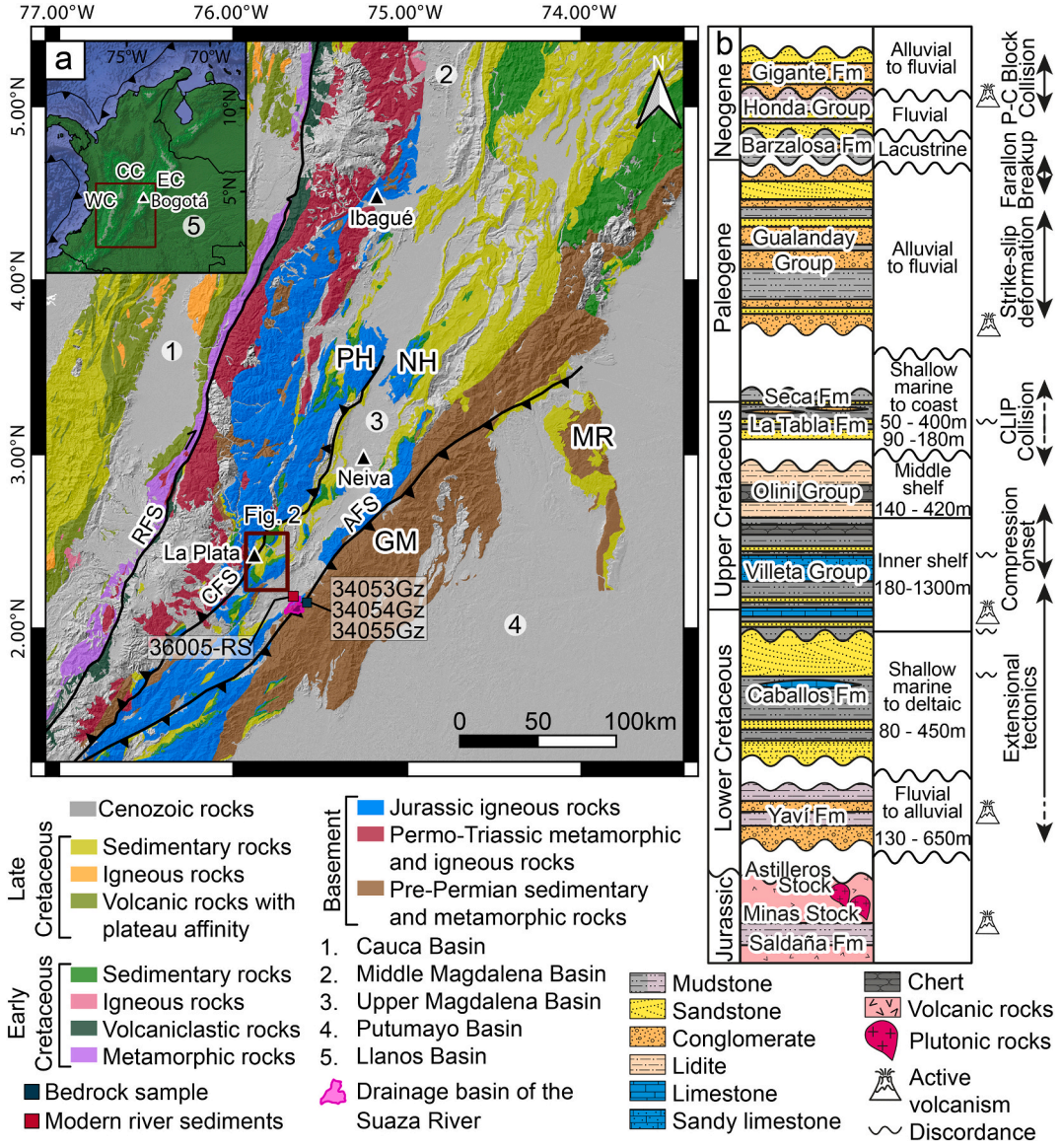

Fig. 1. (a) Geological map showing the Cretaceous and pre-Cretaceous basement units exposed along the Western, Central, and Eastern cordilleras, and the adjacent basins between them. Modified from Gómez and Montes, 2020. The circles with numbers represent the basins. WC = Western Cordillera, CC = Central Cordillera, CE = Eastern Cordillera, RFS = Romeral fault system, CFS = Chusma fault system, AFS = Algeciras fault system, PH = Pata high, NH = Natagaima high, GM = Garzón massif, MR = Macarena range. (b) Chronostratigraphic chart of the Meso-Cenozoic units in the Upper Magdalena Basin, the Cretaceous stratigraphic thicknesses are shown below the sedimentary environment. Labels in the right panel contain interpreted tectonic settings (Spikings et al., 2015; Zapata et al., 2019a). Fm: Formation, P—C Block: Panamá – Choco Block; CLIP: Caribbean Large Igneous Province (Caribbean plateau).

characterized each of these orogenic phases remains an open research topic.

In this contribution, we integrate field observations, stratigraphic, petrographic, and thermo- and geo-chronological data from preserved Cretaceous strata in the Upper Magdalena Basin (UMB) and the adjacent Garzón massif to reconstruct the nature and the timing of the different processes that characterized the Cretaceous extensional and contractional tectonics in the Colombian Andes (Fig. 1a). Our results are interpreted to suggest major changes in the basin configuration and source areas between the Late Jurassic and the Paleocene, this tectonic evolution is an example of the multiple processes that characterize long-lived extensional and contractional settings in Andean-type orogens.

2. Geological setting

2.1. Cretaceous tectonic evolution of the Northern Andes

The Colombian Andes are characterized by an extensive Cretaceous sedimentary record exposed along three northeast-trending ranges – the Western, Central, and Eastern cordilleras – and several hinterland basins such as the Cauca and Magdalena basins (Fig. 1a). The Cretaceous sedimentary strata along the Northern Andes were deposited under contrasting sedimentary environments and tectonic configurations involving continental to marine sedimentation controlled by extensional and contractional tectonic settings (Barrio and Coffield, 1992; Bayona, 2018; Cardona et al., 2020; Mora-Bohorquez et al., 2010; Sarmiento-Rojas, 2019; Sarmiento-Rojas et al., 2006; Zapata et al., 2020; Zapata et al., 2019a).

The Cretaceous to Cenozoic tectonic evolution of the Northern Andes is characterized by an extensional tectonic regime between 145 and 100 Ma, interpreted as a result of major global plate reconfiguration due to the opening of the southern Atlantic Ocean during the Early Cretaceous (Bajolet et al., 2022; Bayona et al., 2006; León et al., 2023; Ramos, 2010; Sarmiento-Rojas et al., 2006; Zapata et al., 2020; Zapata et al., 2019a). Contraction started between ~100 and 80 Ma, marking the onset of the Andean orogeny, where magmatic arcs were built in the west, and foreland basins developed in the east (Cardona et al., 2020; Guerrero et al., 2021; Horton et al., 2010; Jaimes and de Freitas, 2006; Jaramillo et al., 2017; Villagómez et al., 2011; Zapata et al., 2019a). Afterwards, contraction was intensified due to the collision of the Caribbean plateau with the western margin of South America between 72 and 60 Ma, which triggered major topographic growth, deformation, and foreland sedimentation (Bayona et al., 2012; Cardona et al., 2020; Cardona et al., 2012; George et al., 2021; Montes et al., 2019; Mora et al., 2020; Spikings et al., 2015; Villagómez and Spikings, 2013; Vinasco et al., 2006; Zapata et al., 2021; Zapata et al., 2019a).

The Cretaceous sedimentary record of the Colombian Andes can be divided into an eastern and a western domain. Sedimentary basins in the eastern Colombian Andes include the Upper and Middle Magdalena basins, the Eastern Cordillera, and the Llanos Basin (Fig. 1a). The stratigraphic and lithological records of these basins suggest lithospheric stretching between ~145 and ~ 100 Ma, which were characterized by basin deepening and limited magmatic activity (Mora et al., 2006; Sarmiento-Rojas et al., 2006; Vásquez et al., 2010; Villamil, 1999). The western domain includes the Western and Central cordilleras and the Cauca basin; in this region, more intense crustal stretching has been suggested based on the presence of mafic magmatism and ophiolites associated with seafloor spreading between 120 and 100 Ma (Cardona et al., 2020; León et al., 2019; Nivia et al., 2006; Zapata et al., 2019a).

Contractional tectonic settings had different expressions along the Colombian Andes. In the eastern region, the onset of contraction was characterized by marine sedimentation coeval with basin deformation, followed by coarse-grained foreland deposits sourced by intrabasin highs (Bayona, 2018; Bayona et al., 2021; Carvajal-Torres et al., 2022; Jaimes and de Freitas, 2006; Mora-Bohorquez et al., 2010; Valencia-Gómez et al., 2020). In contrast, the western domain of Colombia was characterized by major exhumation and uplift of the Central Cordillera basement with sediment accumulation in a western fore-arc, which is preserved along the Western Cordillera overlying accreted oceanic remnants (Cardona et al., 2020; Spikings et al., 2015; Villagómez et al., 2011; Zapata et al., 2019a). A Paleocene volcanic arc was developed in the Central Cordillera after the collision of the Caribbean plateau (Bayona et al., 2012; Bustamante et al., 2017; Jaramillo et al., 2022; Zapata-Villada et al., 2021).

Finally, Neogene contraction and uplift phases shaped the modern cordilleras. These events are attributed to the collision of the Panamá–Chocó arc and variations in the subduction angle, or changes in the rate and angle of plate convergence vectors (Fig. 1b) (Echeverri et al., 2015; Espitia et al., 2022; Montes et al., 2019; Montes et al., 2015; Mora-Bohorquez et al., 2010; Ramon and Rosero, 2006; Wagner et al., 2017). The normal faults that once bounded the Mesozoic extensional basins in the Eastern Cordillera were reactivated as reverse faults and the basins were inverted, whereas the foreland sedimentation was controlled by diachronous deformation and uplift of intra-basin blocks (Anderson et al., 2016; Bayona et al., 2021; Bayona et al., 2013; Pérez-Consuegra et al., 2021; Cooper et al., 1995; Espitia et al., 2022; Mora et al., 2009; Mora et al., 2006; Ochoa et al., 2012; Saeid et al., 2017; Zapata et al., 2023).

2.2. Stratigraphy of the Upper Magdalena Basin

The UMB in southcentral Colombia includes an extensive Jurassic to Pliocene sedimentary record (Barrio and Coffield, 1992; Cooper et al., 1995). This basin is divided into the Neiva sub-basin to the south of the Pata and Natagaima highs and the Girardot sub-basin to the north (Fig. 1a) (Beltrán and Gallo, 1968; Butler and Schamel, 1988; Ramon and Rosero, 2006). The basement of this basin is mainly composed of Jurassic and Permian igneous rocks, and Precambrian gneisses (the Ibagué batholith, the Páez massif, the Saldaña Formation, the La Plata granite and the Las Minas pluton; Fig. 1a) (De Porta, 1966; Franco and Mojica, 1990; Mora-Bohorquez et al., 2010; Saeid et al., 2017). Two main fault systems bound the Neiva sub-basin, the Algeciras fault system to the east and the Chusma thrust fault system to the west (Fig. 1a; Butler and Schamel, 1988; Franco and Mojica, 1990). These fault systems thrust the basement of the Eastern and Central cordilleras on top of the Cenozoic sequences in the Neiva sub-basin. Paleogene to Neogene deformation has been documented along the Chusma fault (Acosta et al., 2007; Villamizar-Escalante et al., 2021), while Neogene thrusting has been suggested for the Algeciras fault (Anderson et al., 2016; Espitia et al., 2022; Gómez et al., 2005; Saeid et al., 2017).

The Lower Cretaceous sedimentary record in the UMB is represented by the Barremian-Aptian Yaví and Aptian-Albian Caballos formations, which are unconformably overlying the igneous basement. These units consist of coarse-grained strata interbedded with fine-grained facies and limestones accumulated in alluvial to marine-deltaic sedimentary environments (Figs. 1b and 2) (Barrio and Coffield, 1992; Etayo-Serna and Carrillo, 1996; Mejia et al., 2012; Mesa, 2002; Mora et al., 2006; Prössl and Vergara, 1993; Sarmiento-Rojas et al., 2006; Sneider, 1988). The Caballos and Yavi formations have been linked to *syn*-extensional sedimentation based on the relationships between thickness and the depositional environment with normal inverted structures (Mojica and Macía, 1981; Sarmiento-Rojas et al., 2006).

The Yaví and Caballos formations are overlain by fine-grained strata deposited in a shelf environment during the Cenomanian-Campanian stages; this sedimentary succession has been divided into the Cenomanian-Santonian Villeta and the Santonian-Campanian Oliní groups (Fig. 1b) (Guerrero et al., 2020a; Jaramillo et al., 1994; Patarroyo, 2011; Vergara, 1997). The Villeta and Oliní groups are composed of limestones, cherts, mudstones and siliceous siltstones with minor interbedded sandstones and volcanogenic clays (Rubiano-Ortiz, 1989; Sarmiento-Rojas et al., 2006; Terraza-Melo, 2012; Villamil, 1999). Cenomanian to Campanian sedimentation has been interpreted as the

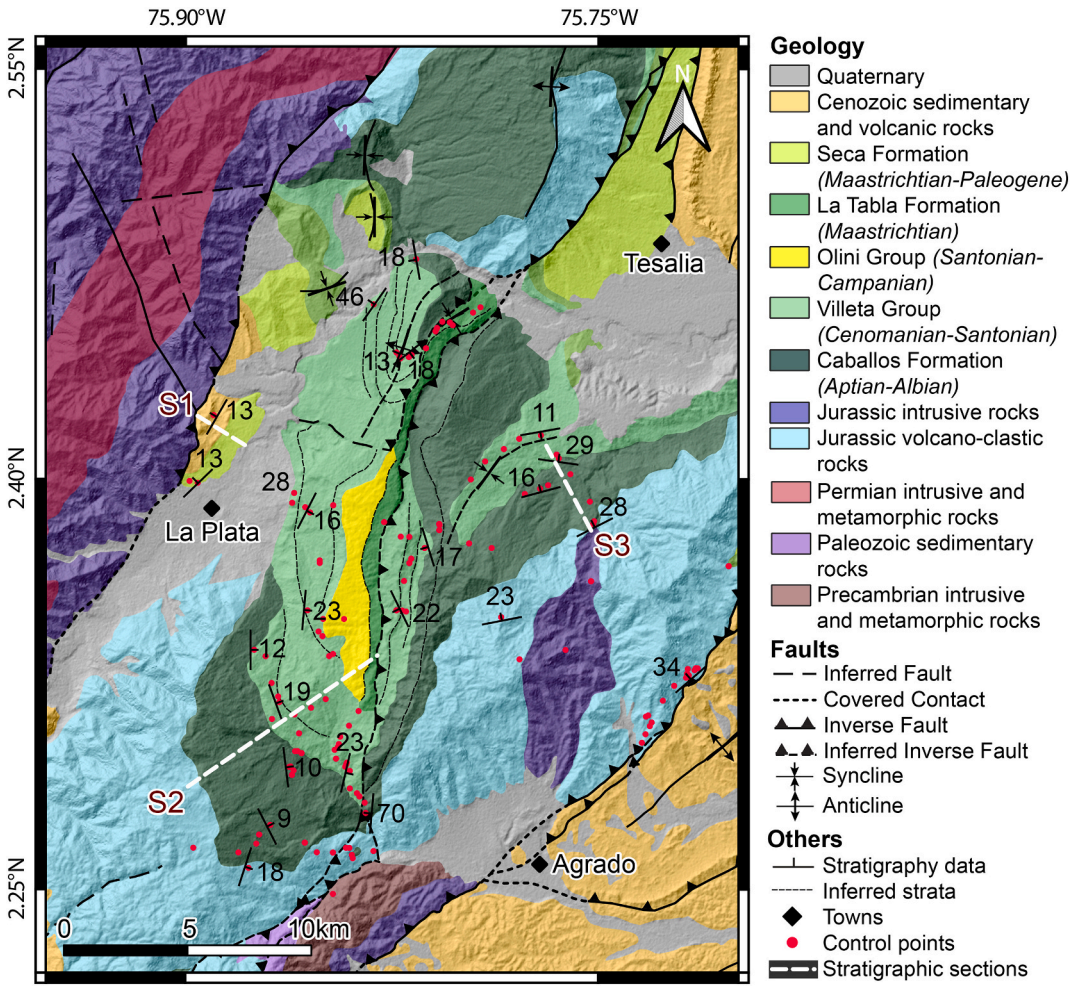

Fig. 2. Geology of the study area with the location of the stratigraphic sections and the control points. The map location is presented in Fig. 1.

result of the post-extensional stage related to the main Cretaceous transgressive cycle in the eastern Colombian Andes and the cessation of regional extension (Barrio and Coffield, 1992; Bayona, 2018). However, seismic data from the Upper and Middle Magdalena basins record contraction events between 100 and 80 Ma (Guerrero et al., 2021; Jaimes and de Freitas, 2006; Van Der Wiel, 1991).

The Upper Cretaceous sedimentary record – the Maastrichtian-Paleocene La Tabla and Seca formations – in the UMB is characterized by the progradation of continental facies over marine facies deposited in shallow marine to coastal environments (Fig. 2) (Barrio and Coffield, 1992; Bayona, 2018; Carvajal-Torres et al., 2022; Carvalho et al., 2021; De Porta, 1966; Julivert, 1968; Mora et al., 2020). The La Tabla Formation is dominated by fine-grained sandstones, whereas the Seca Formation is mainly composed of claystones and pebble-conglomerates. These units were deposited in a foreland setting during and after the onset of the contraction in the Northern Andes (Bayona, 2018; Carvajal-Torres et al., 2022; Mora et al., 2020).

A pronounced angular unconformity between Cretaceous and Eocene clastic rocks is well-preserved in the Magdalena Basin (Fig. 2) (Bayona, 2018; Carvajal-Torres et al., 2022; Gómez et al., 2005; Ramon and Rosero, 2006; Reyes-Harker et al., 2015). During the Cenozoic, sedimentation was dominated by continental environments. The Eocene-Oligocene coarse-grained strata of the Gualanday Group have been associated with alluvial sedimentation sourced by the Central Cordillera (Anderson, 1972; Villamizar-Escalante et al., 2021). The Miocene Barzalosa Formation, the Honda Group, and the Gigante Formation are records of the continental sedimentation in lacustrine, fluvial, and alluvial sedimentary environments in the UMB (Fig. 1b) (Anderson et al., 2016; de La Parra et al., 2019; Gómez et al., 2005; Gómez et al., 2003; Horton et al., 2010; Parra et al., 2012; Reyes-Harker et al., 2015; Zapata et al., 2023).

2.3. *Potential source areas for the Cretaceous strata in the Upper Magdalena Basin*

Evaluation of source areas during basin filling is fundamental for the reconstruction of paleogeography and ancient sedimentary systems (e.g., Decou et al., 2013; Garzanti, 2016; Garzanti et al., 2018; Malusà and Fitzgerald, 2019; Reimann-Zumsprekel et al., 2015; Schneider et al., 2017). The Northern Andes are characterized by contrasting geological domains and distinctive geochronological and lithological signatures, and potential source areas for the Neiva sub-basin include the eastern flank of the Central Cordillera to the west, the Garzón massif and the Amazon craton to the east, and the Natagaima and Pata highs to the north (Fig. 1a) (Horton et al., 2015; Nie et al., 2012).

The metamorphic basement of the Central Cordillera is mainly composed of amphibolites, gneisses, schists, and phyllites, which are characterized by Paleozoic to Jurassic (~540 to 150 Ma) zircon U—Pb age populations, and minor Proterozoic inheritance (~1600 to 1000 Ma) (Bustamante et al., 2017; Naranjo et al., 2018; Ordóñez-Carmona et al., 2006; Villagómez et al., 2011; Vinasco et al., 2006). These rocks were intruded by Permian to Cretaceous plutonic bodies and overlain by volcaniclastic sequences formed in subduction-related magmatic arcs with ages ranging from 300 to 80 Ma (Figs. 1 and 2) (for a more detailed

review see Zapata et al., 2023).

Jurassic plutonic and volcanoclastic rocks are well exposed in the Central Cordillera, Upper and Middle Magdalena basins, and Eastern Cordillera (Fig. 1a) (Bayona et al., 2020; Bayona et al., 2006; Bustamante et al., 2010; Leal-Mejía et al., 2019; Rodríguez-García et al., 2020; Spikings et al., 2015). This magmatic record has been associated with a long-lived magmatic arc between 195 and 150 Ma (Bustamante et al., 2010; Restrepo et al., 2021; Rodríguez-García et al., 2020; Rodríguez et al., 2018; Rodríguez et al., 2016).

Several basement highs bound the UMB, for instance the Natagaima and Pata highs are located to the north of the Neiva sub-basin (Fig. 1a). These basement highs are mainly conformed by Jurassic volcanoclastic rocks (e.g. the Saldaña Formation), that were deposited in a fluvial environment influenced by volcanic products between 200 and 180 Ma (Bayona et al., 1994; Bustamante et al., 2010; Rodríguez et al., 2016; Zapata et al., 2016). These volcanoclastic rocks are intruded by Jurassic plutonic rocks with ages between ~180 and 170 Ma and an emplacement depth of ~4.5 km (Fig. 2) (Bustamante et al., 2016; Bustamante et al., 2010; García-Chinchina, 2018; Rodríguez et al., 2018).

The Garzón massif constitutes the southern portion of the Eastern Cordillera, this basement block contains Paleozoic metasedimentary rocks and Proterozoic granulites and gneisses with zircon U—Pb ages between 1500 and 900 Ma (Ibañez-Mejia et al., 2015; Ibañez-Mejia et al., 2011). These rocks were intruded by Jurassic plutonic rocks with ages between 200 and 160 Ma and are overlain by Jurassic volcanoclastic rocks of the Saldaña Formation (Figs. 1 and 2) (Bustamante et al., 2016; Horton et al., 2010; Ibañez-Mejia et al., 2011, 2015).

The Amazon craton is characterized by Proterozoic gneissic, migmatitic, and granitic units with zircon U—Pb ages of ~1550 Ma and minor alkaline granites formed between 620 and 600 Ma, which are overlain by Paleozoic (~540–440 Ma) sedimentary sequences (Amaya-López et al., 2021; Amaya-López et al., 2020; Ibañez-Mejia et al., 2011). Well data reveals zircon age populations between 1700 and 1450 Ma in deformed granites, gneisses, and amphibolites. To the east, cratonic exposures of felsic granites show Paleoproterozoic ages ranging from 1800 to 1400 Ma, with minor Cretaceous (~100 Ma) mafic dikes (Ibañez-Mejia et al., 2011; Ibañez-Mejia and Cordani, 2020).

Paleozoic sedimentary and metasedimentary rocks are restricted to the UMB, the Garzón massif, and the Amazon craton (Fig. 1a). These units mainly consist of quartz-rich sandstones, mudstones, and limestones that were deposited under marine to transitional conditions (Figs. 1 and 2) (Mojica and Villarroel, 1990; Stibane and Forero, 1969). Biostratigraphic data suggest that these units were deposited between the Ordovician and the Carboniferous (Angiolini et al., 2021; Borrero et al., 2007; Harrington and Kay, 1951; Pastor-Chacón et al., 2023). Zircon U—Pb geochronological analyses from Devonian sedimentary units in the Macarena range (Fig. 1a) yield detrital ages between ~2000 and 1000 Ma, which together with petrographic analyses have been associated with provenance from the Garzón massif and the adjacent Amazon craton (Pastor-Chacón et al., 2023 and references therein).

3. Methods and procedures

3.1. Mapping and stratigraphy

The lithological and stratigraphic features of the Cretaceous sedimentary units were described close to La Plata town (Figs. 1 and 2). Representative samples were selected for petrographic, geo- and thermochronological analysis. Detailed 1:25.000 mapping was carried out to determine structural and stratigraphic relationships (Fig. 2). The locations, geological units, and analytical methods applied for each sample are summarized in Table S1.

Three stratigraphic sections were constructed from the geological map, incorporating facies descriptions derived from approximately 100 control points. The collected samples were projected to the stratigraphic sections. The analysis and interpretation of sedimentary facies and depositional environment were conducted following Miall (1985). The stratigraphic sections were plotted using the package Stratigraphic Data Analysis from R (SDAR) (Ortiz and Jaramillo, 2018).

3.2. Sandstone petrography

Nine sandstones from the Cretaceous units were analyzed. The petrographic analysis was carried out by counting 400 to 500 framework grains, following the Gazzi-Dickinson method (Dickinson, 1985). High-resolution petrographic discrimination of quartz type and metamorphic lithics was performed according to Basu et al. (1975) and Garzanti and Vezzoli (2003). All analyses encompassed the identification of grain types, textural features, and interstitial material (cement, matrix, and pores). Detailed data are presented in Table S2.

3.3. U—Pb Zircon geochronology

Five samples were analyzed using U—Pb zircon geochronology, the analyses were performed for three detrital samples from the Cretaceous strata, one sample from Garzón massif basement, and one from a modern river that drains the Garzón massif (Suaza River; Fig. 1a). Zircon concentrates were obtained from whole rock samples by using a combination of heavy liquid and magnetic separation. The zircon grains were randomly selected in each sample and analyzed via laser ablation inductively coupled plasma mass spectrometry (LA-ICP-MS) at Washington State University, Pullman, United States, following procedures described in Chang et al. (2006). A cutoff of 1000 Ma was applied to select the best age for all single grains. The $^{206}Pb/^{207}Pb$ zircon age is reported for all grains older than 1000 Ma, while the $^{206}Pb/^{238}U$ age is reported for younger grains (Gehrels et al., 2008). The uncertainties are presented in 2-sigma. Detailed data are presented in Table S3. Detailed zircon U—Pb data are fully available in the Geochron database (http://www.geochron.org/dataset/html/geochron_dataset_2023_08_24_dfg2H).

For detrital samples, the analyses were randomly carried on the zircon cores. A discordance filter of 30% for ages older than 500 Ma was used and any ages with analytical uncertainties exceeding 5% were discarded, the Wheterill Concordia diagram is presented in Fig. S1. We used the online software IsoplotR for these plots (Vermeesch, 2018). Kernel Density Estimation (KDE) was obtained for all samples using a bandwidth and bin width of 10 Ma (Vermeesch, 2012). Two different methods were employed to calculate the maximum depositional age (MDA) for each Cretaceous sample: the youngest single grain (YSG) and the weighted average age from the three youngest zircons that overlap at 2σ (Y3Z) (Coutts et al., 2019). The ages used to calculate the YSG and Y3Z correspond to core analyses. The MDA is not presented for detrital samples with zircon U—Pb ages significantly older than the biostratigraphically constrained stratigraphic age.

The Suaza River drains the western flank of the Garzón massif, incorporating sediments derived from metamorphic rocks associated with the Garzón massif, Jurassic volcaniclastic and plutonic rocks, and limited exposure of Lower Cretaceous sedimentary rocks. Additionally, one “in situ” basement sample from the igneous basement in the Garzón massif was analyzed, theses ages were obtained from the zircon cores. Modern sediments and “in situ” basement rocks were sampled to compare ancient and modern zircon U—Pb detrital signature. For the bedrock sample, we applied a discordance filter of 20% for ages older than 500 Ma, and all ages had analytical uncertainties of <2%. The crystallization age was calculated using the weighted average method. The filtered data is presented in a KDE plot and in the Wetherill Concordia diagram (Vermeesch, 2018).

3.4. Low-temperature thermochronology

In five samples, we have implemented the (U-Th-Sm)/He and fission track systems in zircon and apatite to unravel the thermal evolution of

the Garzón massif and the Cretaceous source areas of the UMB. Zircon and apatite mineral concentrates were obtained using standard techniques, including crushing, sieving, and magnetic and heavy liquid separation techniques (Kohn et al., 2019). Zircon grain concentrates for detrital analyses were split into two aliquots, one for ZFT analysis and the other for U—Pb analyses. Thermochronological data are fully available in the Geochron database (http://www.geochron.org/dataset/html/geochron_dataset_2023_08_24_dfg2H).

3.4.1. Zircon and Apatite Fission Track dating (ZFT and AFT)

The spontaneous fission of ^{238}U induces linear damage in the crystal lattice of apatite (AFT) and zircon (ZFT). These linear damage zones are known as tracks. The quantification of these tracks can be used to infer the time passed since they began to be preserved within the mineral lattice (e.g., Fleischer et al., 1975; Galbraith and Laslett, 1993; Green, 1981; Tagami and O'Sullivan, 2005; Wagner and Van den Haute, 1992). The temperature intervals at which tracks can be partially annealed are known as the zircon and apatite partial annealing zones, ZPAZ and APAZ, respectively (Wagner et al., 1989).

The kinetics of the ZFT system are still poorly understood; however, in typical geological settings with cooling rates of ~15 °C, the closure temperature (Tc) for the ZFT is ~240 ± 30 °C and the ZPAZ is between 180 and 220 °C (Brandon et al., 1998; Bernet, 2009; Bernet and Garver, 2005). However, laboratory- and field-based studies have suggested that the Tc could be as low as 180 °C or as high as 350 °C (Bernet, 2009; Rahn et al., 2019; Tagami et al., 1998; Yamada et al., 2007). These differences in the Tc have been attributed to the effect of radiation damage: low-damage grains are more resistant to annealing than high-damage grains (Bernet, 2009; Garver et al., 2005). Low-damaged zircons could be annealed at ~180–200 °C, and high-retentive zircons could be fully annealed at temperatures above 300 °C (Garver et al., 2005).

The APAZ is between 60 and 120 °C (Gleadow and Duddy, 1981; Reiners and Brandon, 2006). The kinetics of the apatite crystals depends mainly on the chemical composition of the grains (F-apatites are low-retentive, whereas Cl-apatites are high-retentive). The track resistance to annealing, is proportional to the resistance of the crystal to the acid used to reveal the tracks (etching). Thus, the size of the fission-track etch pit (Dpar) is a commonly used proxy for annealing resistance in thermal history modeling (Carlson et al., 1999; Donelick et al., 1999).

The fission-track analyses were performed at the Low-Temperature Thermochronology Laboratory (LabTer) of the São Paulo University. ZFT ages were obtained on 104 to 60 zircons from three detrital samples from the Cretaceous strata in the study region, and ZFT and AFT analyses were conducted on 10 apatites and 24 zircons from a bedrock sample from the Garzón massif, using the External Detector Method (EDM) (Gleadow and Duddy, 1981). 2σ errors are reported for all ages. The Chi-Square test (P(χ2)) was used to determine whether individual grain ages correspond to a single population (Galbraith and Laslett, 1993). Detailed procedures for etching and sample preparation are presented in Text S1. The detailed ZFT and AFT data are available in Tables S4 and S5, respectively. Additionally, Fig. S2 presents a comparison between the uranium content measured in the zircons dated by U—Pb geochronology and the uranium content calculated in the zircons dated by ZFT thermochronology.

Radial and probability density plots were used to visualize the age distribution of the detrital and bedrock samples (Vermeesch, 2018). Radial plots were created using the IsoplotR software (Vermeesch, 2018), and for the detrital samples, the major age population peaks were extracted using the binomial peak fitting method and the Binomfit software (Brandon, 1996; Galbraith and Laslett, 1993). The Binomfit software (Brandon, 1996) was chosen because it provides an iterative search of peak ages, the number of peaks, and the width bin (of the histogram) to find the simplest solution that fits the dataset.

3.4.2. Zircon and Apatite (U-Th-Sm)/He dating (ZHe and AHe)

U-Th-Sm/He thermochronology is based on the production, accumulation, and diffusion of helium resulting from the alpha decay of U, Th, and Sm. In typical geological settings, the zircon U-Th-Sm/He (ZHe) dating provides insight into the thermal history between 140 and 220 °C, and the apatite U-Th-Sm/He (AHe) between 40 and 110 °C. These temperature intervals are known as the zircon partial retention zone (ZPRZ) and the apatite partial retention zone (APRZ) (Farley, 2002; Flowers, 2009; Reiners, 2005). However, the temperature sensitivity of the ZHe could be as low as ~50 °C in zircons that have been subjected to very high radiation damage (Ault et al., 2018; Gautheron et al., 2022; Gérard et al., 2022; Guenthner et al., 2013; Johnson et al., 2017). The APRZ and ZPRZ depend on the effective uranium content (eU = 0.235*Th + U), grain size, and geometry, the cooling rate, and the accumulation of the radiation damage in the crystal lattice (e.g., Anderson et al., 2020; Brown et al., 2013; Guenthner et al., 2013).

ZHe and AHe analyses were performed on two samples from the basement of the Garzón massif. Four euhedral and inclusion-free zircon grains were selected from each sample and packed into ~1 mm Nb tubes. Four apatite crystals were hand-picked from one of the samples and packed into ~1 mm Pt tubes using a binocular microscope. The dimensions of the selected grains were measured, and their morphology was described to calculate the α-correction (Ft correction) (Farley, 2002; Farley et al., 1996).

The analyses followed the procedures presented by Zhou et al. (2017) for AHe and Zapata et al. (2019b) for ZHe. Grain degassing was conducted at the Alphachron laboratory at the Potsdam University, while the measurement of U, Th, and Sm concentrations was carried out at the German Research Center of Geoscience (GFZ). Detailed data are presented in Table S6.

3.4.3. Thermal modeling

To extract the most probable thermal history from the thermochronological data, we used the Bayesian statistics implemented in the QTQt software (Gallagher, 2012). For ZHe data, we used the radiation damage model from Guenthner et al. (2013), while for the AHe data, we used the model from Flowers (2009). The AFT data were modeled with the annealing model from Ketcham et al. (2007), and the ZFT data were modeled with the annealing model from Yamada et al. (2007). The models included only the U-Th-Sm/He single-grain aliquots with reproducible ages or dispersed ages with possible size or eU age controls. Reproducible U-Th-Sm/He ages were defined as aliquots with a 1σ standard deviation <20% of the mean age (Ault et al., 2019; Flowers et al., 2023). In the absence of correlations between grain size or -eU and age, the overdispersed aliquots were removed from the model. A total of 500,000 iterations were used to search for possible model solutions (200,000 of the burn-in phase and 300,000 in the post-burn-in phase), the model was allowed to find solutions (including complex solutions) between 0 and 200 Ma in a temperature range of 0 to 400 °C. The likelihood chain is shown in Fig. S3.

A geological constraint was included in the model to represent the crystallization age of the Precambrian syenogranite (sample 34055Gz), which yields ages between 1500 and 1000 Ma, the constraint was set to 1000 ± 10 Ma at 380 ± 10 °C. The complete thermal history model is presented in Fig. S4.

Additionally, two sensitivity tests were performed to assess the effect of the excluded AHe aliquots and the effect of the radiation damage in zircons on the final thermal history model (Abbey et al., 2023). Therefore, an alternative thermal history model that included the younger apatite U-Th-Sm/He ages is presented in Fig. S5. To evaluate the impact of the different Tc of the ZFT system due to the radiation damage, we also include an alternative model without the ZFT data, in which instead an additional constraint was included to represent fully reset ZFT data at lower temperatures (99 ± 14 Ma at 240 ± 60 °C) (Fig. S6).

4. Results

4.1. Stratigraphy

The Cretaceous record of the UMB was described in three different stratigraphic sections that include thirteen sedimentary facies and five facies associations (Tables 1 and 2). Sections 1 and 2 were described in the western part of the basin, whereas section 3 corresponds to the eastern segment (Fig. 3).

4.1.1. Lower Cretaceous Caballos Formation

The Aptian-Albian Caballos Formation is presented in sections 2 and 3 (Figs. 2a and 3). It was observed laying in angular unconformity on top of the Jurassic volcaniclastic rocks of the Saldaña Formation (Fig. 1) and in non-conformity on the Jurassic quartz-monzodiorite of the Astilleros Stock (section 3). In both stratigraphic sections, this unit is constituted by the facies association I, which is dominantly composed of laterally discontinuous and channeled massive conglomerates and sandstones (Gm and Sm), with a thickness between 1 and 2 m. Occasionally layers of massive sandstone (Sm) facies may exhibit coal lenses (C; subbituminous), sandstones with cross and trough-cross lamination (Sc and St), and planar-laminated and graded sandstones (Sp). These facies are interbedded with tabular dark gray massive and planar-laminated mudstones (Fm and Fp). Lateral variations in stratigraphic thickness were observed in the two sections: in the west, the Caballos Formation is ~250 m thick in section 2, while to the east (section 3), this unit is up to ~720 m thick (Fig. 3).

The facies St, Sp, and Sc are generated by bedload deposition of confined unidirectional currents (Miall, 1985; Shiers et al., 2018). The facies Sm and Gm are associated with unconfined hyper-concentrated flows that allow a rapid deposition during abrupt changes in flow velocity (Horn et al., 2017). The fine-grained facies (Fm and Fp) resulted from the deposition of suspended load (Table 1) (Collinson et al., 2006).

The facies assemblage I is interpreted as part of an alluvial fan system, where the coarse-grained beds represent deposition under unidirectional confined currents (St, Sc, and Sp) and unconfined high-density flow (Gm and Sm). The presence of coal lenses in the Sm facies suggests an upper-flow regime with periods of low energy and anoxic or low-oxygen conditions (Miall, 1985; Shanley et al., 1992). The Fm and Fp facies are the record of floodplain deposition related to the deposition of suspended sediments during low-energy conditions (Nichols, 2009). The preserved lamination suggests continuous subaqueous deposition (Fig. 3; Table 2) (Turner and Tester, 2006).

This facies assemblage is consistent with sedimentary environments suggested in other stratigraphic sections of the Caballos Formation in the Upper Magdalena and Putumayo basins, where fluvial and alluvial to marine–deltaic environments have been recognized (Barrio and Cofield, 1992; Mesa, 2002; Mora et al., 2006; Mora-Bohorquez et al., 2010; León et al., 2023; Sarmiento-Rojas et al., 2006; Sneider, 1988).

4.1.2. Upper Cretaceous Villeta Group

The Cenomanian-Santonian Villeta Group conformably overlies the Caballos Formation (Fig. 3). Facies association in this unit (Facies II) is predominantly composed of black planar-parallel laminated and massive calcareous mudstones (Fp and Fm), wackestones, and sandy limestones (W and Ls), interbedded with black massive calcareous sandstones (Sm) (Tables 1 and 2). This facies association is characterized by tabular and laterally continuous beds with sharp contacts, ranging

Table 1
Description and interpretation of sedimentary facies.

Code	Facies	Description	Interpretation
Gm	Massive conglomerate	Structureless pebble to granule matrix-supported conglomerate	Fast deposition of high-density flows (Collinson et al., 2006; Miall, 1977)
Gp	Plane-parallel laminated conglomerate	Pebble to granule matrix-supported conglomerate with planar-parallel lamination	Deposition of a high-flow regime (Collinson et al., 2006; Miall, 1977)
Sm	Massive sandstone	Structureless very fine- to coarse-grained sandstones, in some cases calcareous sandstones	Rapid deposition of hyper-concentrated load during abrupt changes in flow speed (Collinson et al., 2006; Horn et al., 2017)
Sp	Plane-parallel laminated sandstone	Medium- to coarse-grained sandstone with planar-parallel lamination	Rapid deposition of diluted high-energy flows. Normal grading suggests fluctuations in the flow regime (Collinson et al., 2006; Kumar et al., 2007)
Sc	Cross-bedded sandstone	Medium- to coarse-grained sandstone with cross-bedded stratification	Deposition by 2D migration bedforms under unidirectional flows (Miall, 1985; Shiers et al., 2018)
St	Trough cross-bedded sandstone	Medium- to coarse-grained sandstone with trough stratification	Deposition by 3D dunes migration under unidirectional flows (Collinson et al., 2006; Miall, 1977)
Fm	Massive mudstone	Structureless black to gray siliciclastic and calcareous mudstones, in some cases with calcareous nodules or concretions up to 1 m in diameter	Deposition of fine-grained suspended load in anoxic or low-oxygen conditions (Collinson et al., 2006)
Fmr	Massive mudstone	Structureless red siliciclastic mudstones with calcareous nodules	Deposition of fine-grained suspended load in oxidizing conditions (Collinson et al., 2006; Voigt et al., 2013)
Fp	Plane-parallel laminated mudstone	Black to gray siliciclastic and calcareous mudstones with horizontal lamination	Deposition of fine-grained suspended sediment in low-energy conditions (Collinson et al., 2006)
Fsi	Siliceous siltstone	Gray and beige siliceous siltstones with horizontal lamination organized in tabular beds	Deposition of fine-grained suspended sediments in low-energy conditions with siliceous fluids during diagenesis (Randon and Caridroit, 2008)
C	Coal	Coal lenses	Flood plains with abundant organic material deposited under anoxic or low-oxygen conditions (Miall, 1985)
Ls	Sandy limestone	Fine-grained dark gray siliciclastic limestone	Deposition of carbonates with input of fine-grained siliciclastic sediments in clam-water (Nichols, 2009)
W	Wackestone	Gray wackestone with scarce and float allochems in a micritic matrix	Deposition of carbonate sediments in-situ in calm-water influenced by biological processes (Dunham, 1962)

Table 2
Facies association description and interpretations of the depositional system.

Facies association	Constituent facies	Description	Interpretation
Facies association I	Gm, St, Sc, Sp, Sm, Fm, Fp, C	Confined and unconfined high-density flows in subaqueous conditions interbedded with fine-grained deposits from the overbank	Alluvial sedimentation characterized by high-energy flows adjacent to a well-developed flood plain
Facies association II	Sm, Fm, Fp, Ls, W	Shallow-marine carbonate deposits characterized by fine-grained and carbonate sedimentation interbedded massive underflows	Shallow-marine carbonate sedimentation in the inner- to mid-shelf with mixed carbonate-clastic sedimentation
Facies association III	Fp, Fsi	Shallow-marine fine-grained sedimentation characterized by siliceous diagenesis	Shallow-marine sedimentation in an outer-shelf
Facies association IV	Sm, Sp, Fm	Sandy shelf with reworking by wave processes and, confined and unconfined high-density flows	Shallow-marine sedimentation dominated by siliciclastic deposits
Facies association V	Gp, Gm, Sc, Sp, Sm, Fmr	Beaches with accumulation of coarse-grained sediments from drainages of rivers that laterally transition to fine-grained coastal plains with oxidizing conditions	Coastal plain highly influenced by run-off from fluvial processes

from 0.1 to 1 m in thick and organized in 2 to 5 m stacked packages.

Section 2 can be divided into two segments: the lower segment is composed mainly of calcareous mudstones interbedded with wackestones and some calcareous sandstones, and the upper segment is characterized by an increment of calcareous sandstones (Fig. 3).

The calcareous mudstones and wackestones (Fp, Fm, and W) are related to deposition under low-oxygen and low-energy marine conditions (Collinson et al., 2006; Nichols, 2009). The calcareous sandstones and sandy limestones (Sm and Ls) are interpreted as ephemeral underflows that resulted in mixed calcareous-clastic sedimentation (Table 1) (Flood et al., 2009).

The facies association II described in the Villeta Group is interpreted as being deposited in a shallow marine environment, where the increase in coarse-grained sedimentation towards the top indicates a shallowing-upward trend (Nichols, 2009). This association is characterized by black calcareous mudstones interbedded with wackestones and sandy limestones, which were deposited in the inner- to mid-shelf areas under low-energy and low-oxygen conditions. The upward increase of the Sm facies in the upper segment of section 2 suggests an increase in detrital sediment input during the accumulation of this unit (Fig. 3).

Our results are consistent with previous studies of the Villeta Group suggesting deposition in a shallow marine environment under anoxic conditions with shallower deposition towards the top (Barrio and Coffield, 1992; Guerrero et al., 2000; Vergara, 1997).

4.1.3. Upper Cretaceous Oliní Group

The Santonian-Campanian Oliní Group was described in section 2, where it conformably overlies the Villeta Group (Fig. 3). This unit is constituted by the facies association III, which is composed of light-gray planar-parallel laminated mudstones and black-to-beige siliceous siltstones (Fp and Fsi). These beds are tabular, with sharp bedding and centimeter-scale lamination, and are laterally continuous, and organized in stacked packages of 1 to 5 m (Tables 1 and 2).

Facies association III is interpreted as deeper-marine sedimentation in contrast to facies association II, where sedimentary deposition occurred predominantly under low-energy and subaqueous conditions. The sharp stratification between light and dark beds suggests relatively sudden events superimposed on a background of quiet and continuous sedimentation of the finer-grained layers (Table 2) (Collinson et al., 2006). This interpretation agrees with previous studies that have used the presence of chert, siliceous siltstones and phosphorites, as well as the foraminiferal assemblage to suggest an outer shelf for the Oliní Group (Barrio and Coffield, 1992; Guerrero et al., 2000; Vergara, 1997).

4.1.4. Upper Cretaceous La Tabla Formation

The Maastrichtian La Tabla Formation conformably overlies the Oliní Group and is composed of facies association IV. This facies assemblage is characterized by laterally discontinuous and tabular 1 to 3 m thick massive and planar-laminated sandstones of beige color (Sm and Sp), interbedded with tabular massive mudstones of light-gray color (Fm).

Massive and planar-laminated sandstones (Sm and Sp) are the result of high-energy confined and unconfined currents (Turner and Tester, 2006). The amalgamated coarse-grained beds are generated by combined flows (Sm and Sp), including confined and unconfined high-density flows (Collinson et al., 2006). The fine-grained facies (Fm) resulted from the deposition of suspended load (Table 1) (Collinson et al., 2006).

Facies assemblage IV is interpreted to be deposited within a sandy shelf. These conditions are intercalated with deposition in ephemeral overbank areas under oxidizing conditions (Fm) (Nichols, 2009; Noel and Robert, 2010). This interpretation is consistent with sedimentary environments proposed in other stratigraphic sections of the La Tabla Formation to the north (Barrio and Coffield, 1992; Bayona, 2018; Carvajal-Torres et al., 2022; Guerrero et al., 2000; Martín-Rincón et al., 2022; Veloza et al., 2008; Vergara, 1997).

4.1.5. Upper Cretaceous Seca Formation

The Maastrichtian-Paleocene Seca Formation was described in stratigraphic section 1 (Fig. 3). This unit overlies the La Tabla Formation and underlies the Gualanday Group (Figs. 1b and 3) (Bayona, 2018; Carvajal-Torres et al., 2022).This unit is constituted by facies association V, which is mainly composed of gray to beige massive conglomerates and sandstones (Gm and Sm), planar-laminated conglomerates and sandstones (Gp and Sp), and sandstones with cross lamination (Sc), interbedded with tabular red massive mudstones (Fmr) containing calcareous nodules (Tables 1 and 2). This facies association exhibits laterally discontinuous, amalgamated, and tabular beds with thicknesses between 1 and 3 m.

Massive sandstones and conglomerates are associated with the rapid deposition of hyper-concentrated load during abrupt changes in flow velocity (Collinson et al., 2006; Horn et al., 2017). Whereas the conglomerates and sandstones with tractive structures (Gp, Sp, and Sc) resulted from the deposition of sediment transported as bedload by unidirectional currents (Collinson et al., 2006; Miall, 1985; Shiers et al., 2018). The red fine-grained mudstones (Fmr) suggest the deposition of suspended load under oxidizing conditions (Collinson et al., 2006; Voigt et al., 2013).

This facies assemblage is interpreted as the result of different depositional processes within a coastal plain environment highly influenced by fluvial processes (Nichols, 2009). The coarse-grained facies with tractive structures and amalgamated facies architecture are products of bedload deposition by unidirectional currents (Bridge, 2003). These flows vary laterally into overbank areas, where sedimentation of suspended load under oxidizing conditions prevailed. The massive structure of the fine-grained beds and the development of calcareous nodules

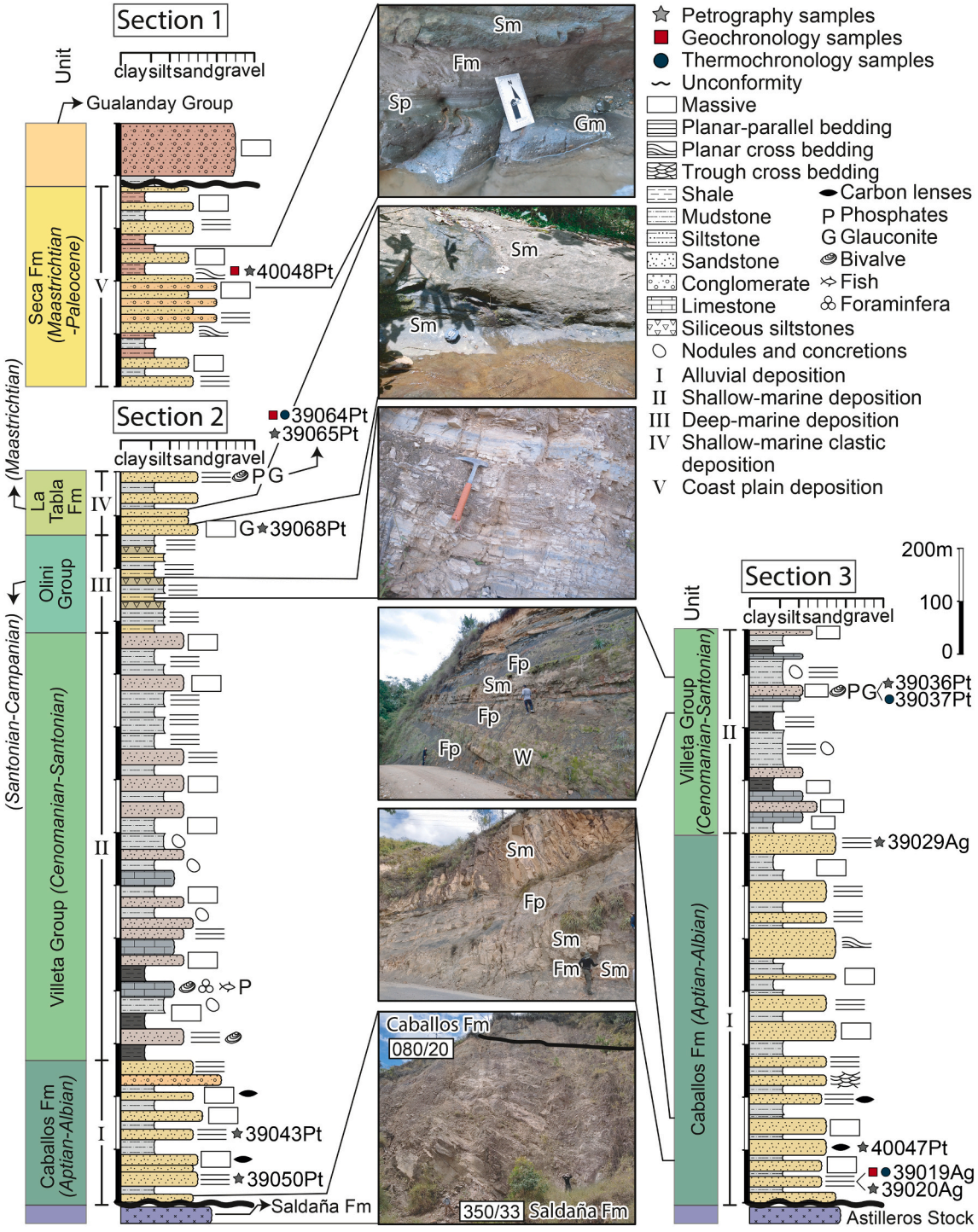

Fig. 3. Stratigraphic sections with sedimentary facies photographs. The stratigraphic position of the petrography (gray stars), detrital geochronology (red squares), and detrital thermochronology (blue dots) samples are also presented. The locations of the stratigraphic sections are presented in Fig. 2. For the lithology color scheme, refer to Table 1. (For interpretation of the references to color in this figure legend, the reader is referred to the web version of this article.)

suggest periods of subaerial exposure characteristic of an intermittent water body (McPherson, 1979; Voigt et al., 2013).

In the Upper and Middle Magdalena basins, stratigraphic and lithological studies have already suggested fluvial to coastal plains and fluvial environments for the accumulation of the Seca Formation (Barrio and Coffield, 1992; Bayona, 2018; Carvajal-Torres et al., 2022; Guerrero et al., 2000).

4.2. Petrography

Sandstones from the Aptian-Albian Caballos Formation consist of fine- to coarse-grained subangular to subrounded grains embedded in a clay-rich matrix. The sandstone composition is characterized by 55% to 96% of quartz, feldspar varies between 2% and 16%, and the lithic fraction is up to 16%. Lithics are predominantly sedimentary, and low- and medium-grade metamorphic (Table 3, Fig. 4a, b). In section 2, the sandstones from the Caballos Formation are classified as lithic arkose

Table 3
Summary of the petrographic analysis in the studied sandstones. Qm: monocrystalline quartz; Qpf: foliated polycrystalline quartz; Qpp: Polygonal polycrystalline quartz; Qpd: diffuse polycrystalline quartz; Pl: plagioclase; Fk: potassium feldspar; F: undifferentiated feldspar. Detailed data are presented in Table S2.

Unit	Sample	Quartz				Feldspar			Lithics			Other minerals
		Qm	Qpf	Qpp	Qpd	Pl	Fk	F	Metamorphic	Sedimentary	Volcanic	
	39020Ag	92.8	0.0	1.4	2.0	0.0	0.0	2.0	0.0	0.0	0.0	1.8
	39029Ag	73.1	0.0	0.6	11.7	0.2	0.6	1.3	2.1	7.7	0.0	2.7
Caballos Fm	39043Pt	45.9	0.6	0.3	11.6	0.3	0.9	16.1	4.6	12.2	0.0	7.6
	39050Pt	58.4	0.5	0.3	3.6	0.5	0.0	6.4	6.1	9.2	0.0	15.1
	40047Pt	79.9	0.4	0.4	7.7	0.7	0.2	0.7	3.5	3.8	0.0	2.7
Villeta Group	39036Pt	73.4	0.0	0.2	0.2	2.8	1.8	0.0	1.4	0.2	0.0	19.9
La Tabla Fm	39065Pt	71.3	0.0	0.2	0.8	5.3	2.0	7.1	0.2	0.6	0.0	12.5
	39068Pt	77.3	0.2	0.2	0.2	4.1	1.8	4.3	0.6	1.4	0.0	10.0
Seca Fm	40048Pt	6.4	0.8	0.0	3.3	2.5	0.0	6.6	6.6	58.3	8.2	7.2

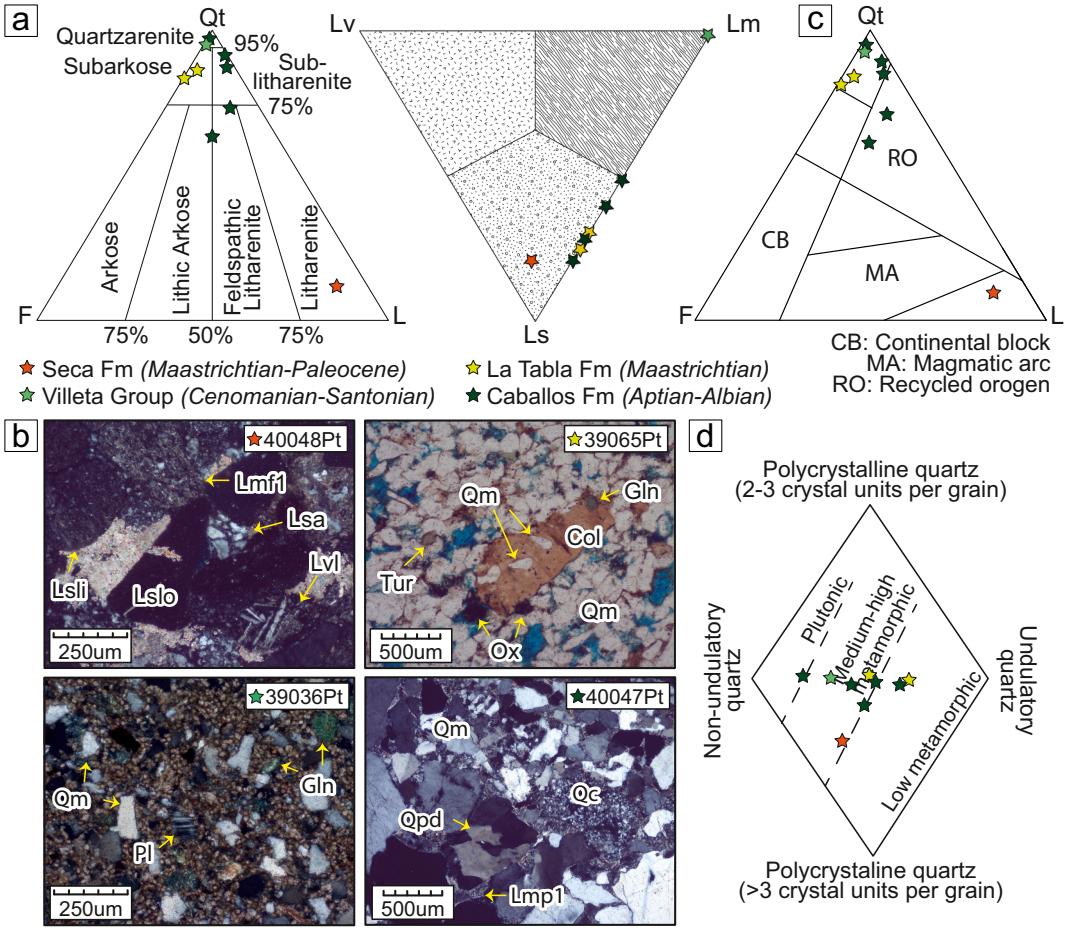

Fig. 4. Petrography results. (a) Sandstone classification QFL diagram after Folk (1980), and lithic abundance diagram. (b) Photomicrographs from the Caballos Formation (40047Pt), the Villeta Group (39036Pt), the La Tabla Formation (39065Pt), and the Seca Formation (40048Pt); blue-colored epoxy was used to highlight rock porosity. (c) Sandstone provenance discrimination diagram QFL according to Garzanti (2016). (d) Quartz classification after Basu et al. (1975). Qt: total quartz, Qm: monocrystalline quartz, F: feldspar, L: lithics, Lv: volcanic lithics, Lm: metamorphic lithics, Ls: sedimentary lithics, Qpd: diffuse polycrystalline quartz, Qc: Chert, Pl: plagioclase, Gln: glauconite, Tur: tourmaline, Col: collophane, Ox: oxides, Lsli: siltstone, Lslo: mudstone, Lsa: sandstone, Lvl: lathwork volcanic lithic, Lmp1: Slate lithic fragment, Lmf1: Meta-siltstone lithic fragment. Thin-section images are shown in cross-polarized light (40047Pt, 39036Pt, and 40048Pt), and in transmitted light (39065Pt). (For interpretation of the references to color in this figure legend, the reader is referred to the web version of this article.)

and feldspathic litharenite, whereas the sandstones of section 3 exhibit variations between quartzarenite and sub-litharenite (Fig. 4a). The metamorphic lithic fragments include pelitic and psammitic/felsic protoliths. A sandstone from the Cenomanian-Santonian Villeta Group (39036Pt) presents a micritic matrix, and the siliciclastic grains are mainly composed of non-undulatory monocrystalline quartz and plagioclase (Fig. 4a, b), furthermore, authigenic minerals such as glauconite and collophane are present in the sample with a proportion of 7% (Fig. 4b). Samples from both the Caballos Formation and the Villeta Group plot within the recycled orogen field (Fig. 4c). The quartz fraction in all sandstones consists mainly of monocrystalline and polycrystalline quartz, with >3 crystals per grain (Fig. 4d).

Two sandstones from the Maastrichtian La Tabla Formation correspond to very fine- to fine-grained subarkoses with subrounded to rounded grains embedded in a clay-rich matrix (Fig. 4a). The sandstone composition is characterized by ~73% of quartz, predominantly

composed of undulatory monocrystalline quartz, the feldspar content varies between 10% and 14% (Fig. 4a, d). The lithic fraction is up to 2% and consist mainly of sedimentary and low- to medium-grade metamorphic lithics. The sedimentary lithics include mudstones, siltstones, and cherts, and the metamorphic lithic fragments are solely represented by a felsic protolith (Table 3, Fig. 4a). In the provenance discrimination diagram, the samples plot within the recycled orogen field (Fig. 4c). Authigenic minerals such as glauconite and amorphous nodular collophane are present at ~5% (Fig. 4b).

Finally, a sample from the Maastrichtian-Paleocene Seca Formation corresponds to a fine- to medium-grained litharenite with subangular to subrounded grains embedded in a clay-rich matrix (Fig. 4a). This sample is characterized by 73% of lithics, 9% quartz, and 8% of feldspar (Table 3). The lithic fraction is mainly composed of sedimentary and volcanic lithics (59% and 8% respectively), with a minor proportion of low- to medium-grade metamorphic lithics (6%). Within the sedimentary lithics mudstone, siltstone, and chert fragments predominate, while the volcanic lithic fragments include mainly lathwork (3%) and microlithic (5%) lithics. The metamorphic lithics include pelitic and felsic protoliths, with similar proportions (Fig. 4b). The provenance discrimination diagram, the sample plot within the lithic recycled field (Fig. 4c), and the quartz fraction in this sample consist mainly of polycrystalline quartz with >3 crystals per grain (Fig. 4d).

4.3. Zircon U—Pb Geochronology

Zircon U—Pb geochronology was performed on three sandstones from the Caballos, La Tabla, and Seca formations, together with a bedrock sample from the Proterozoic basement of the Garzón massif and one from modern river sediments (Figs. 2 and 3). A moderately deformed syenogranite with an inequigranular medium- to coarse-grained texture from the Garzón massif (34054Gz) shows zircon U—Pb ages between 1515 and 850 Ma, with uranium contents varying between 146.2 and 1025.0 ppm and have Th/U ratios between 0.09 and 0.42, suggesting an igneous origin (Harley and Kelly, 2007; Rubatto, 2002). Zircons are subhedral to euhedral in shape, with grain sizes ranging between 50 and 300 μm, and length:width (l:w) ratios between 1:1 and 3:1. The Wetherill Concordia diagram shows a possible lead loss in the dated zircons, evidenced by a line with a lower intercept at 843 ± 21.2 Ma and an upper intercept at 1569.2 ± 10.1 Ma, (MSWD of 8.9). The upper intercept is interpreted to represent the crystallization age (Fig. 5a).

Detrital ages of 108 zircon grains from modern sand sediments (sample 36005-RS) range from 1517 to 166 Ma. This sample is

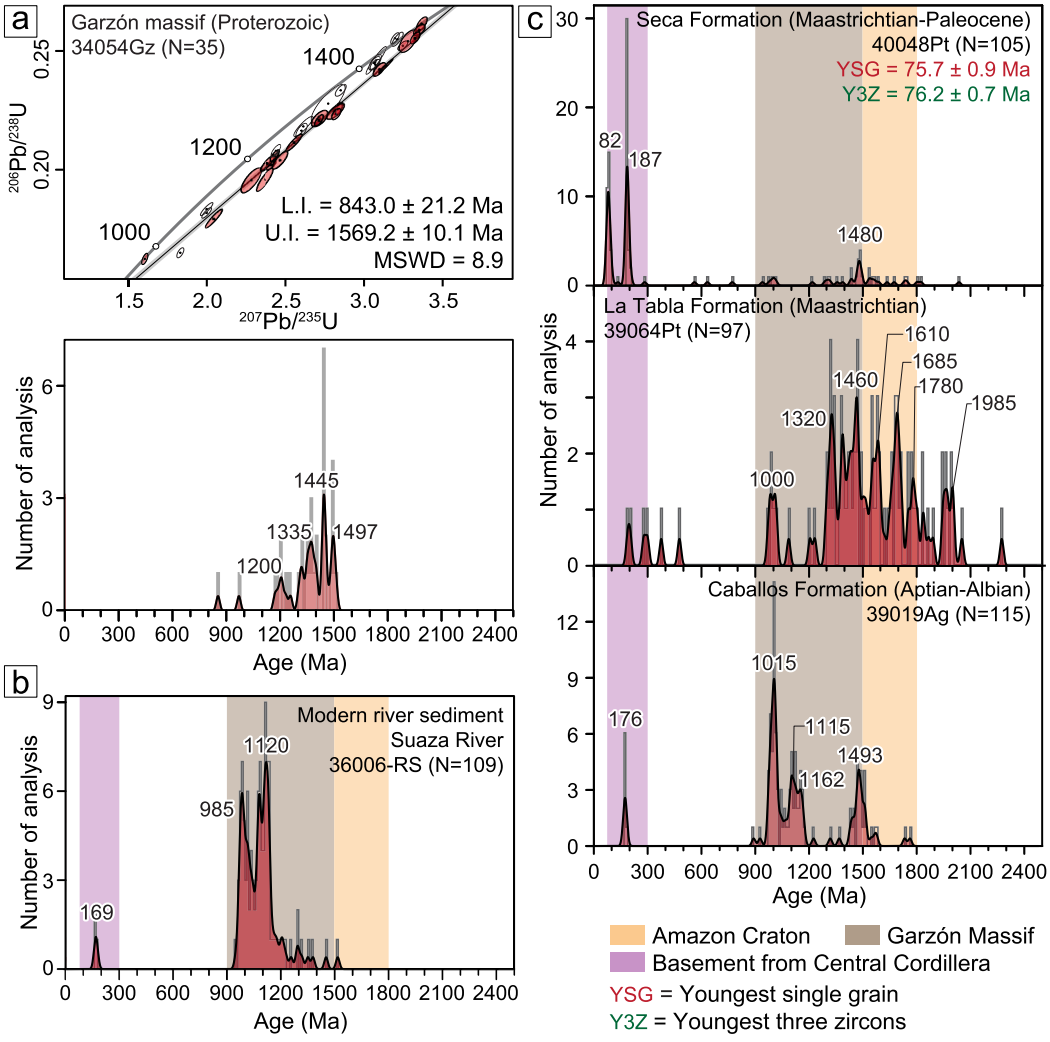

Fig. 5. Zircon U—Pb geochronological results (a) Wetherill Concordia diagram and Kernel Density Estimation plot (KDE) for the sample from the Garzón massif. L.I: Lower intercept, U·I: Upper intercept. (b) KDE for the detrital zircon U—Pb geochronology of modern river sediments from the Suaza River. (c) KDEs showing the results of the detrital zircon U—Pb geochronology results from samples of the Cretaceous strata (the Caballos, La Tabla, and Seca formations). YSG: Youngest single grain, Y3Z: weighted average of the three youngest grains. The location of the samples is shown in Figs. 2 and 3.

characterized by major Proterozoic age peaks (1200 to 980 Ma; 87% of the grains), and a minor Jurassic age peak of 169 Ma (Fig. 5b). The bedrock sample 34054Gz shows ages between 1500 and 1100 Ma. Modern sediments and bedrock samples evidenced the diagnostic 1500 to 900 Ma signature of the Garzón massif (Horton et al., 2015).

A total of 115 individual zircon U—Pb ages were obtained from the Aptian-Albian Caballos Formation. Major age peaks are of Proterozoic (1600 to 1000 Ma) age, with >90% of the grains; a minor Jurassic age peak of 176 Ma is also present. (Table 4; Fig. 5c). Measured uranium concentrations range from 9.5 and 2032.0 ppm, with 64% of the zircon grains having uranium lower than 150 ppm (Table S3; Fig. S2).

A total of 97 detrital zircons from a sandstone sample of the Maastrichtian La Tabla Formation were analyzed. Most of these zircons have U—Pb ages older than 900 Ma, 8% of the grains are between 1200 and 900 Ma, 36% are between 1500 and 1200 Ma, and 50% are older than 1500 Ma (Table 4; Fig. 5c). The uranium content varies between 55.2 and 3250.0 ppm, with 22% of the zircon grains having uranium lower than 150 ppm (Table S3; Fig. S2).

A total of 105 zircon U—Pb ages were obtained from one sample of the Maastrichtian-Paleocene Seca Formation. This unit exhibits two major age peaks of Jurassic (187 Ma) and Cretaceous (87 Ma) age, which correspond to ~65% of the ages. Additionally, Proterozoic age peaks correspond to ~32% of the ages. The youngest single zircon in the unit corresponds to 75.7 ± 0.9 Ma (Table 4; Fig. 5c). Measured uranium concentrations range from 29.1 to 1555.0 ppm (Table S3).

4.4. Low-temperature thermochronology

Two samples of deformed Proterozoic granitoids exposed on the western flank of the Garzón massif (34055Gz and 34053Gz, Tables 5 and 6, Fig. 2a) were analyzed by ZFT, ZHe, AFT and/or AHe. Detrital ZFT data were obtained from three Cretaceous samples, including the Aptian-Albian Caballos Formation (39019Ag), the Cenomanian-Santonian Villeta Group (39037Pt), and the Maastrichtian La Tabla Formation (39064Pt).

4.4.1. Bedrock low-temperature thermochronology and inverse thermal modeling

ZFT dating was performed on 24 zircon grains from sample 34055Gz, which was collected on the eastern flank of the basin (Fig. 1a). This sample has individual ZFT ages between 166.4 and 69.4 Ma, with uranium content between 122.9 and 334.6 ppm. This sample has a pooled age of 98.7 ± 13.5 Ma, with a P(χ^2) value of 0.95 (Table 5; Fig. 6a).

ZHe dating was performed on two samples (34055Gz and 34053Gz) from the Garzón massif (Table 6; Fig. 1a). Sample 34053Gz has four zircon ages between 87.8 ± 8.7 and 35.1 ± 1.8 Ma, three of which have reproducible ZHe ages, with a mean age of 73.3 ± 13.7 Ma. ESR values are between 60.8 and 71.4 μm, and eU values vary from 246.8 to 1449.6 ppm (Fig. 6b). Finally, two zircons were dated in sample 34055Gz, with ages of 115.5 ± 6.5 and 94.4 ± 4.2 Ma; these zircons yield reproducible ZHe ages with a mean age of 105.0 ± 14.9 Ma. ESR values are 46.1 and 52.6 μm, and the eU values are 437.7 and 1472.4 ppm (Fig. 6b).

Sample 34055Gz had a poor apatite recovery, therefore, AFT dating was performed on 10 grains, with single crystal AFT ages are between 15.7 and 7.9 Ma, with uranium content between 41.9 and 95.2 ppm, and a mean Dpar of 2.0 μm. The age distribution has a pooled age of 12.1 ± 1.8 Ma, with a P(χ^2) value of 0.80 (Table 5; Fig. 6a).

Four AHe ages from sample 34053Gz are between 24.6 ± 0.6 and 8.5 ± 0.5 Ma, three of which yield reproducible ages, with a mean age of 22.6 ± 2.4 Ma. ESR values are between 55.1 and 64.6 μm, and eU values vary from 107.2 to 218.6 ppm. The AHe ages exhibit a positive correlation between age and grain size (Table 6; Fig. 6b).

The inverse thermal history model was obtained from the two samples collected within the Garzón massif and included three AHe aliquots with ages between 24.6 and 20.0 Ma, five aliquots of ZHe with ages between 115.5 and 71.7 Ma, the AFT age (12.1 Ma) and the ZFT age (98.7 Ma) from sample 34055Gz (Tables 5 and 6; Fig. 6c). Since the thermochronological ages are younger than 100 Ma, the model is poorly constrained between 180 and 100 Ma and does not offer information on the thermal evolution of the Garzón massif during this time. After 100 Ma, the thermal history model exhibits rapid cooling between ~100 and 85 Ma, followed by isothermal conditions at ~50 °C between 85 and 35 Ma, a reheating between ~35 and 20 Ma, and a final cooling event at ~20 Ma. This model reproduces the observed AHe, AFT, and ZFT ages with an age difference of <8 Ma, the predicted ages of ZHe show discrepancies up to 20 Ma compared to the observed data (Fig. 6c).

Alternative thermal models are presented in Figs. S5 and S6, incorporating the younger apatite U-Th-Sm/He ages and replacing the ZFT data with a geological constraint. The results of this model show a similar thermal history, with all models showing ~100 and 80 Ma cooling, minor reheating between 80 and 25 Ma, and cooling between 25 and 15 Ma. These results suggest that the excluded aliquots and the implemented ZFT annealing model did not have a significant influence in the interpreted thermal trajectories.

4.4.2. Detrital ZFT thermochronology

Detrital ZFT ages were obtained on 104 grains from a sandstone sample of the Aptian-Albian Caballos Formation (39019Ag) located in section 3 (Fig. 3). This sample has single-grain ZFT ages between 710.2 and 98.9 Ma, with uranium contents varying from 16.9 to 152.2 ppm, a data dispersion of 39%, and P(χ^2) value of 0.03. (Fig. 7a). Deconvolution of the peak ages using Binomfit software (Brandon, 1996) shows that the sample can be interpreted as two detrital ZFT age signatures of 155.3 ± 41.7 Ma (39.6%) and 260.4 ± 67.4 Ma (60.4%) (Table 5; Fig. 7b).

ZFT analyses were performed on 60 zircon grains from the Cenomanian-Santonian Villeta Group (39037Pt) located in section 3 (Fig. 3). This sample has single grain ZFT ages between 263.6 and 79.2 Ma, with uranium contents between 45.2 and 325.5 ppm, data dispersion of 0%, and a P(χ^2) value of 1.0 (Fig. 7a). Deconvolution of the peak ages reveals a single population at 153.0 ± 19.3 Ma (Table 5; Fig. 7b).

Sample 39064Pt from the Maastrichtian La Tabla Formation was collected in section 2 (Fig. 3). This sample has 88 individual grains with

Table 4
Summary of the detrital geochronological results with the age ranges in percent for the detrital samples. Detailed data are presented in Table S3.

Lithostratigraphic Unit	Lithology and stratigraphic age	N (grain number)	Ages (%)					
			0–- 150 Ma	150–- 300 Ma	300–- 900 Ma	900–- 1200 Ma	1200–- 1500 Ma	>1500 Ma
Suaza River (36005-RS)	Modern river sediments	109	0.0	2.7	0.0	87.2	9.2	0.9
Caballos Fm (39019Ag)	Sandstone (Aptian-Albian)	115	0.0	6.1	0.9	65.2	14.8	13.0
La Tabla Fm (39064Pt)	Sandstone (Maastrichtian)	114	0.0	4.1	2.1	8.2	36.1	49.5
Seca Fm (40048Pt)	Sandstone (Maastrichtian-Paleogene)	105	29.5	35.2	2.9	4.8	16.2	11.4

Table 5
Summary of detrital and bedrock fission track results. The bedrock ZFT and AFT ages correspond to the pooled ages and detrital ZFT ages correspond to the best-fitting component ages, calculated with the peak age routine in the Binomfit software (Brandon, 1996).

Sample ID	Type	Mineral	Nb*	Ns	Ni	Nd	RhoS	RhoI	RhoD (x10^5)**	Age ± 2σ (Ma)	Peak percentage	P(χ2) (%)	Dpar ± 2σ (μm)
34055Gz	Syenogranite	Apatite	10	217	3204	18,252	1.09E+06	1.60E+07	35.878	12.1 ± 1.8		79.8	1.97 ± 0.15
		Zircon	24	2822	275	9354	2.13E+07	2.07E+06	1.203	98.7 ± 13.5		95.5	
39019Ag	Sandstone	Zircon	115	13,896	792	9354	1.35E+07	7.71E+05	1.361	(P1) 155.3 ± 41.7 (P2) 260.4 ± 67.4	39.6% 60.4%	2.9	
39037Pt	Sandstone	Zircon	60	5359	354	9354	1.44E+07	9.52E+05	1.272	(P1) 153.0 ± 19.3	100%	99.8	
39064Pt	Sandstone	Zircon	93	6250	407	9354	1.09E+07	7.07E+05	1.226	(P1) 159.6 ± 19.4	100%	83.8	

* Number of counted grains.
** Dosimeter track density.

Table 6
Single-grain Apatite and Zircon (U—Th— Sm)/He data. Red letters denote the aliquots excluded from the inverse thermal model presented in Fig. 6c.

Sample ID-aliquot		Age (Ma)	± 2σ (Ma)	U (ppm)	Th (ppm)	Sm (ppm)	eU (ppm)	He (nmol/g)	mass (ug)	Ft	ESR (um)*	Tm**
aHe	34053Gz-a1	8.5	0.2	134.5	136.5	395.8	170.3	5.9	2.05	0.75	58.4	2
	34053Gz-a2	23.3	0.4	158.4	235.7	495.9	218.6	21.2	2.07	0.77	64.6	2
	34053Gz-a3	20.0	0.2	96.7	222.1	370.2	152.6	12.2	2.36	0.75	55.1	1
	34053Gz-a4	24.6	0.2	71.0	140.8	318.1	107.2	11.1	3.12	0.78	63.4	1
zHe	34053GZ-z1	60.3	0.3	1420.3	123.3	1.7	1449.6	392.3	9.89	0.83	66.0	2
	34053GZ-z2	87.8	0.6	240.0	28.8	0.5	246.8	95.8	7.49	0.81	60.8	2
	34053GZ-z3	35.1	0.3	404.4	199.0	0.2	451.8	71.9	10.58	0.84	71.4	2
	34053GZ-z4	71.7	0.5	562.2	60.5	1.1	576.6	182.5	7.66	0.81	60.8	2
	34055GZ-z2	94.4	0.9	1436.5	150.7	4.3	1472.4	594.3	5.58	0.79	52.6	2
	34055GZ-z4	115.5	1.2	394.7	178.0	2.4	437.1	207.4	3.59	0.76	46.1	2

* ERS: equivalent spherical radius.
** Terminations.

ZFT ages between 388.1 and 68.7 Ma, uranium content between 26.8 and 140.7 ppm, data dispersion of 0% and a P(χ^2) value of 0.8 (Fig. 7a). Deconvolution of the peak ages shows a single population at 159.6 ± 19.4 Ma (Table 5; Fig. 7b). Overall, all samples contained several grains with track densities too high (e.g. metamict grains), in which the spontaneous tracks could not be counted.

Fig. S2 presents a comparison of the uranium content obtained from ZFT thermochronology and zircon U—Pb geochronology, showing that the uranium content obtained from ZFT analyses is more constrained than that from U—Pb analyses. However, both methods include low-uranium zircons. In the U—Pb measurements, all zircon age populations include zircons with low U zircons. For instance, in the Caballos Formation, 64% of the zircons in the U—Pb analyses have U concentrations <150 ppm and correspond to Jurassic and Proterozoic ages.

5. Discussion

Two broad tectonostratigraphic scenarios dominated the Cretaceous evolution of the Northern Andes: an Early Cretaceous extensional setting, which has been interpreted as rift- and back-arc-related tectonics. This phase was followed by Late Cretaceous contractional tectonics associated with changes in the subduction configuration and terrane collision (Bayona, 2018; Bayona et al., 2012; Cardona et al., 2020; Cardona et al., 2012; Montes et al., 2019; Mora et al., 2020; Mora-Bohorquez et al., 2010; Sarmiento-Rojas et al., 2006; Spikings et al., 2015; Zapata et al., 2020; Zapata et al., 2019a). These tectonic models have discriminated broad time intervals in which tectonic activity took place, however, the pre-Cretaceous tectonic settings that preceded the Cretaceous extensional phases and a precise discrimination of the extensional and contractional settings remain to be resolved. Our results present the opportunity to refine the temporality and discriminate the different processes that characterize each of the above-mentioned tectonic scenarios.

5.1. Late Jurassic to Early Cretaceous setting in the UMB (160 to 120 Ma)

Obtained detrital ZFT peak ages from the Aptian to Maastrichtian units in the UMB range between 153 and 260 Ma, showing a strong Late Jurassic component at ~155 ± 20 Ma, which is observed in the P1 of the Caballos Formation, and the central ages of the samples from the Villeta Group and the La Tabla Formation (Fig. 7).

The ZFT ages from the Cretaceous strata contrast with the detrital zircon U—Pb signature that reveals major Proterozoic age populations (between 2000 and 1000 Ma) and a minor Jurassic peak age at ~176 Ma (Fig. 8a). The zircon grains used for fission-tracks contain relatively low uranium (<150 ppm) that overlap with 64% of the U—Pb ages obtained in the Caballos Formation and 22% in the La Tabla Formation. High uranium grains that are not present in the ZFT data were likely not suitable for fission-track thermochronology due to the high track densities. Poorly represented low uranium grains in the ZFT results may introduce an additional bias; however, all major zircon U—Pb populations in the Caballos and La Tabla formations contain a proportion of low uranium grains, which may reduce this bias effect.

The significant difference between the U—Pb and ZFT detrital signatures, together with the similar uranium concentrations obtained from the ZFT and U—Pb analyses (Fig. S2), could suggest that most ZFT ages are the result of the cooling of the source areas rather than being associated with a volcanic source or post-magmatic cooling (Malusà and Fitzgerald, 2019). However, the relatively low zircon-uranium content of the analyzed samples resulted in large single grain ZFT age errors and unimodal detrital age populations with a large 2-sigma interval, which may not reflect the geological complexity (Galbraith, 2005; Malusà and Fitzgerald, 2019).

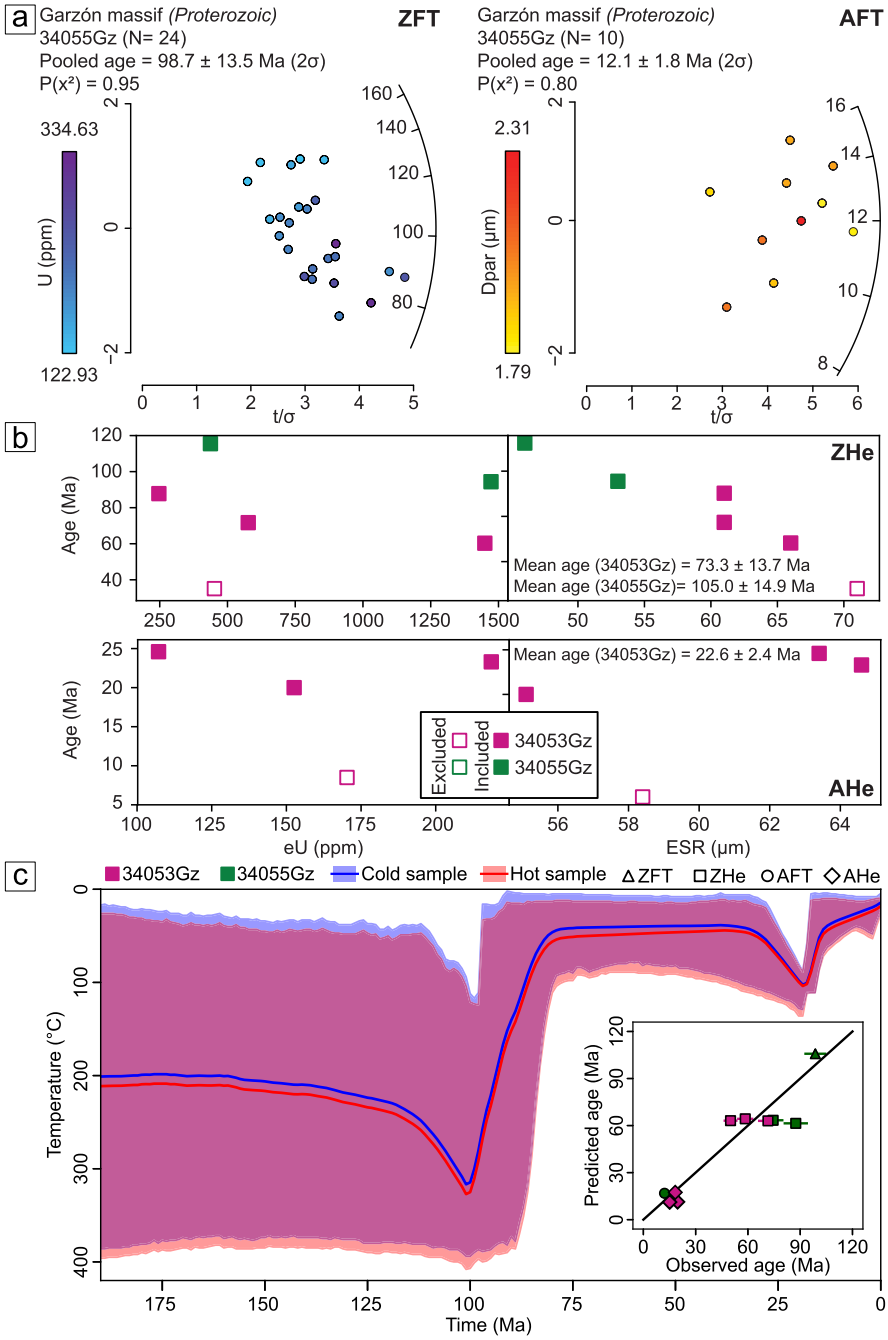

Fig. 6. Bedrock thermochronological results from the Garzón massif samples. (a) Radial plot showing the distribution of ZFT and AFT single-grain ages from sample 34055Gz, color code denotes single grain uranium content for ZFT and single grain Dpar for AFT. (b) Effective uranium (eU) vs. age, and grain size (equivalent spherical radius: ESR) vs. age plots of ZHe and AHe ages. The color code denotes the sample, and the hollow markers indicate the aliquots excluded from the inverse thermal history models. (c) Inverse thermal history model from the bedrock data collected on the western flank of the Garzón massif. Observed age vs. predicted age, with samples indicate by marker color, and marker shape denoting the thermochronological system. The complete thermal history model is presented in Fig. S4.

Available vitrinite reflectance measurements (%Ro) below 0.5 have been obtained from the Caballos Formation in the Neiva sub-basin, these values suggest maximum burial temperatures between 86 and 95 °C for this unit (Burnham and Sweeney, 1989; Mann and Stein, 1997; Roncancio and Martinez, 2011). Consequently, the studied segment of the Caballos Formation had not reached the ZPAZ after deposition, indicating that the acquired ZFT ages are likely the result of source area exhumation rather than partial resetting during burial. The presented ZFT data provide evidence for Late Jurassic to Early Cretaceous exhumation in the Northern Andes – an exhumation history that is poorly preserved in the basement due to Late Cretaceous and Cenozoic orogenic erosion (Horton et al., 2015; Horton et al., 2010; Li et al., 2022; Mora et al., 2020; Parra et al., 2020; Villamizar-Escalante et al., 2021; Zapata et al., 2020). For instance, thermochronological ages from the Garzón massif basement, which are younger than 100 Ma, result in a poorly constrained Jurassic to Early Cretaceous thermal history (Fig. 6c).

The ZFT age peaks between ~155 ± 19.3 and ~ 159 ± 19.4 Ma obtained from the Cretaceous units in the UMB can be explained by either Late Jurassic contractional exhumation, Early Cretaceous extension, or a combination of both. Unfortunately, as discussed above, the

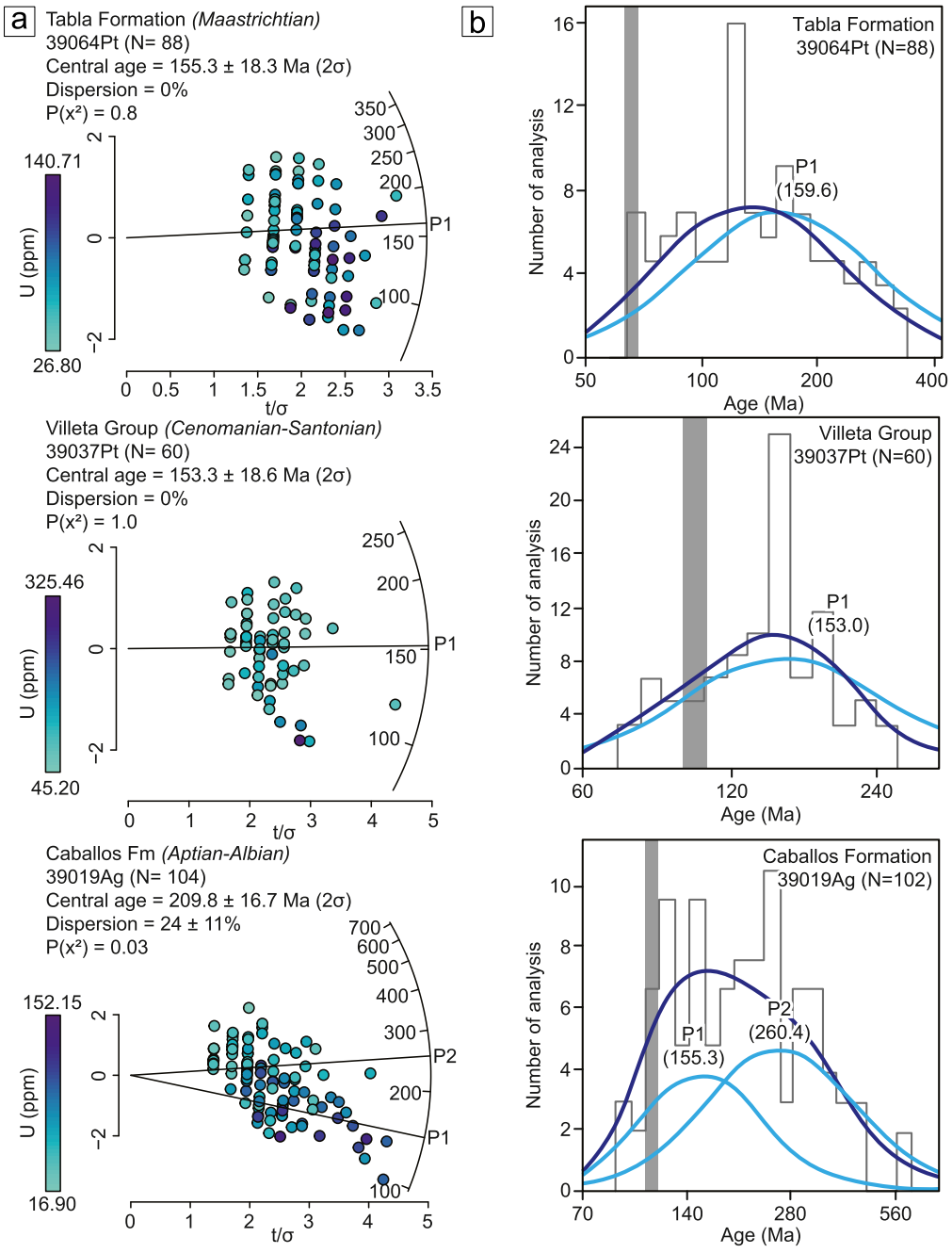

Fig. 7. Detrital ZFT thermochronological results. (a) Radial plots show the distribution of the single-grain detrital ages, and the color code denotes single-grain uranium content. Radial plots were made with Isoplot R, black lines represent the peak age populations calculated with Binomfit (Brandon, 1996; Vermeesch, 2018). (b) Kernel density estimation plots were calculated with Binomfit, dark-blue lines denote the probability distribution, and the light-blue lines represent the modeled age peaks (Brandon, 1996). The gray lines represent the depositional age of the Cretaceous sedimentary units. (For interpretation of the references to color in this figure legend, the reader is referred to the web version of this article.)

ZFT data do not have the resolution to distinguish between these events. However, field mapping delimited an unconformity between the Aptian-Albian Caballos Formation and the deeply crystallized (>2 km) Jurassic plutonic rocks (e.g. Astilleros pluton; Fig. 3) (García-Chinchina, 2018), which is evidence for Late Jurassic to Early Cretaceous deformation and exhumation in the UMB. This event has also been proposed based on regional metamorphism between ~163 and 153 Ma (Blanco-Quintero et al., 2014; Restrepo et al., 2021; Rodríguez-García et al., 2020).

After the Late Jurassic deformation in the UMB, a shift towards a regional extensional setting started during the Early Cretaceous, resulting in the development of normal faults and the deposition of the Barremian-Albian Yaví and Caballos formations (Mora et al., 2009; Mora et al., 2006; Sarmiento-Rojas, 2019; Sarmiento-Rojas et al., 2006). The onset of extensional tectonics partially overlaps with the obtained ZFT detrital data, and thus, it may have also contributed to the observed exhumation signals. Moreover, Early Cretaceous ZFT ages sourced from the Central Cordillera and preserved in Late Cretaceous strata in NW Colombia further support the possibility of regional Early Cretaceous exhumation (Zapata et al., 2020).

Despite the existence of evidence for Late Jurassic to Early

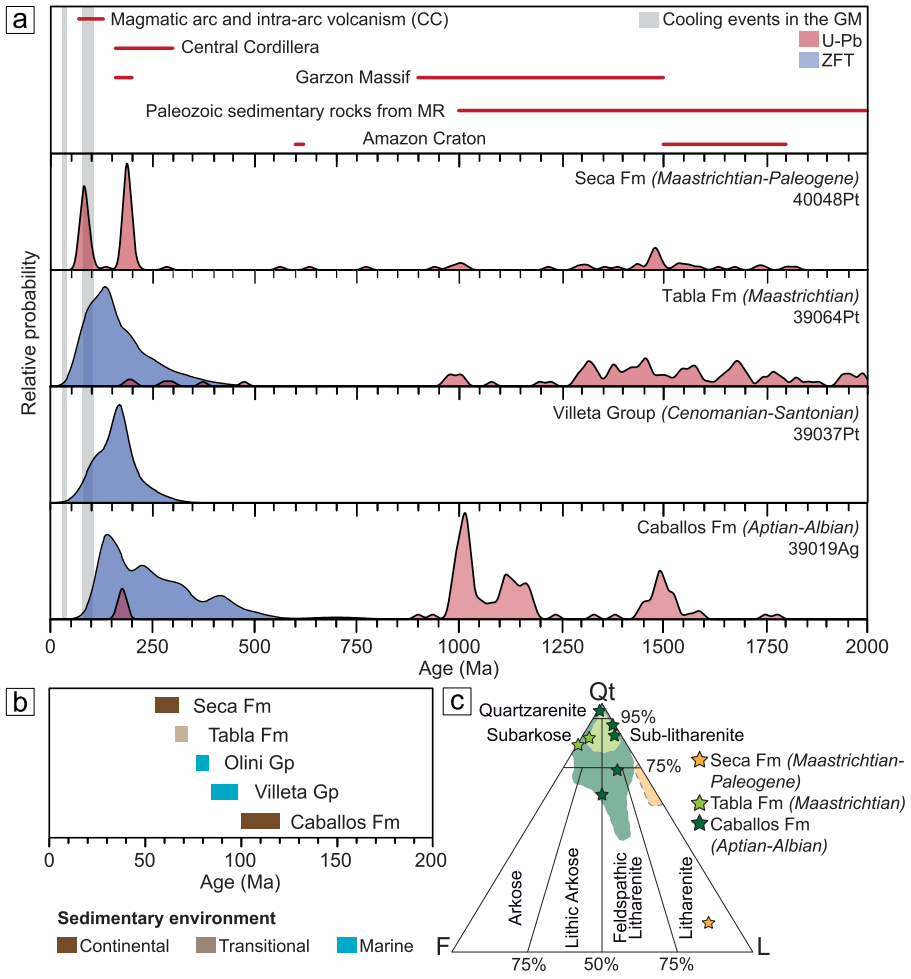

Fig. 8. (a) Comparison between the zircon U—Pb geochronological and ZFT data of the Cretaceous strata obtained in this work. KDE of zircon U—Pb geochronology (red) and ZFT (blue) from the Cretaceous units. Gray vertical bars denote the Cretaceous and Miocene cooling events unraveled in the thermal history of the Garzón massif (GM; Fig. 6c). Red horizontal lines denote the zircon U—Pb geochronological signatures of the potential source areas including the Amazon craton, Paleozoic sedimentary rocks from the Macarena range, the Garzón massif, the Central Cordillera, and the Cretaceous magmatic arc and associated volcanoclastic rocks (Bustamante et al., 2010; Horton et al., 2010; Ibañez-Mejia et al., 2011, 2015; Pastor-Chacón et al., 2023; Zapata et al., 2019a). (b) sedimentary depositional system and depositional ages of the Cretaceous units of the UMB, horizontal bars summarize the age assignments for each unit (Bayona, 2018; Etayo-Serna and Carrillo, 1996; Julivert, 1968; Prössl and Vergara, 1993; Vergara, 1997). (c) compiled sandstone petrographic data, stars denote petrography present in this study and the shaded areas correspond to previous studies (Duarte et al., 2018; Gómez et al., 2003; León et al., 2023; Mesa, 2002; Veloza et al., 2008). (For interpretation of the references to color in this figure legend, the reader is referred to the web version of this article.)

Cretaceous deformation, the extent and spatial distribution of exhumation during each event, along with their respective contributions to regional basement exhumation, remain as unresolved and open research questions. This deformation event has also been documented by a Cretaceous discordance in the northern Peruvian Andes, where it has been associated with major plate reorganization and transpressional reactivation of older structures (George et al., 2019).

The onset of *syn*-extensional sedimentation in the northern basins started between 145 and 130 Ma in the north of the UMB and the Eastern Cordillera (Mora et al., 2009; Mora et al., 2006; Sarmiento-Rojas, 2019; Sarmiento-Rojas et al., 2006) (Fig. 1). The absence of a contemporaneous sedimentary record in the southern segment of the UMB (Mora-Bohorquez et al., 2010) could suggest that this basin was not a significant depocenter or the basin experienced a period of non-deposition during the Early Cretaceous (~145–120 Ma; Fig. 9). The lack of a sedimentary record in the UMB was probably related to doming and uplifts, as is common in early extension-related phases (Cloetingh et al., 2013; Huismans et al., 2001).

5.2. *Pronounced Early Cretaceous extensional phase (120 to 100 Ma) in the UMB*

The extensional history of the UMB is documented by integrating field observations, petrographic, and detrital zircon geochronology. An extensional stage occurred between ~120 and ~ 100 Ma, as evidenced by the onset of extensional sedimentation in the Aptian-Albian Caballos Formation. The stratigraphic sections and facies described for the Caballos Formation suggest a sedimentary environment related to an alluvial system associated with well-developed floodplains (Figs. 3 and 8b).

Lateral variations in stratigraphic thickness of up to ~500 m in <10 km were observed between sections 2 and 3 of the Caballos Formation (Fig. 3), similar to what has been documented in other segments of the UMB (Mora-Bohorquez et al., 2010; Sarmiento-Rojas, 2019). Thickness and facies variations are common in extensional settings and can be explained by syn-deformational sedimentation coeval with normal fault activity, with higher stratigraphic thickness proximal to the structures (Brune et al., 2023; Destro, 1995; Liesa et al., 2006; Mora et al., 2009). The sedimentation recorded by the Aptian-Albian Caballos Formation would have been related to normal fault activity on the eastern side of

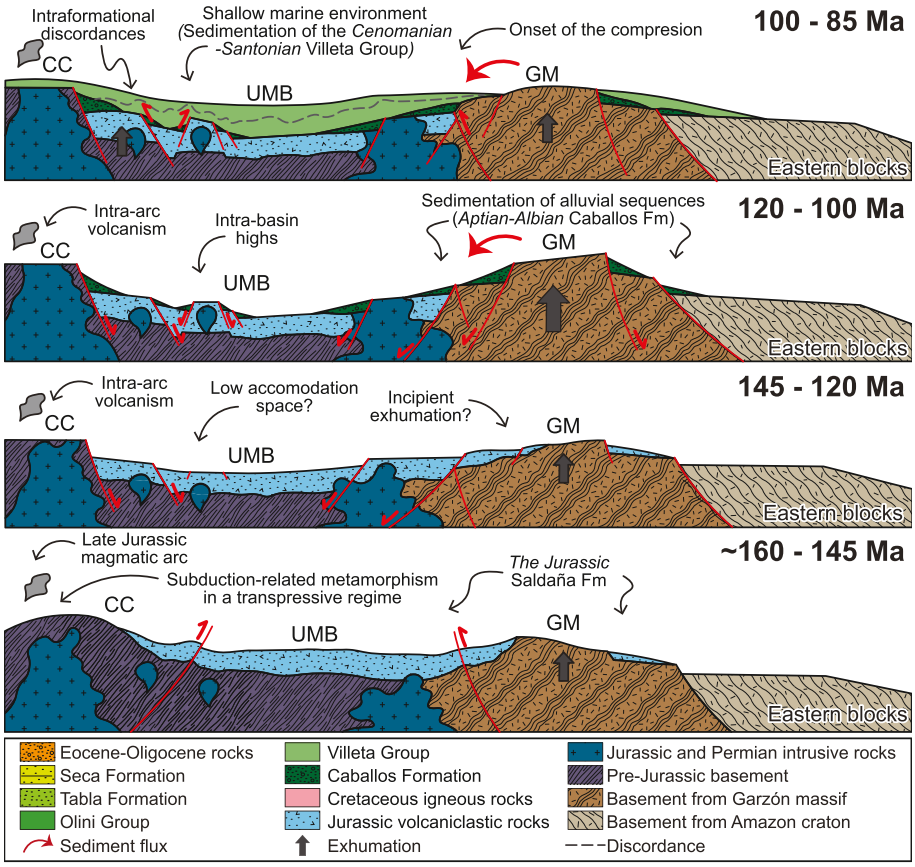

Fig. 9. Schematic model for the tectonic evolution of the Upper Magdalena Basin showing possible configurations that would explain the geo- and thermochronological data from the Cretaceous sedimentary rocks and the thermal history of the Garzón massif between ~160 and 85 Ma. CC = Central Cordillera, UMB = Upper Magdalena Basin, GM = Garzón massif.

the mapped area (Garzón massif and blocks in the Amazon craton), where the stratigraphic thickness of this unit is higher (Mora-Bohorquez et al., 2010). These normal fault controls on sedimentation have also been observed in seismic data from the UMB (Mora et al., 2006, 2009; Mora-Bohorquez et al., 2010; Sarmiento-Rojas, 2019).

Detrital zircon U—Pb age populations from the Caballos Formation suggest that rocks related to the Garzón massif were the main source area in this segment of the basin (Fig. 1). This interpretation is supported by the similar age populations of the Caballos Formation and the geochronological data from the Garzón massif. Modern river sediments from the Suaza River, which drains the Garzón massif, show Proterozoic (1200–980 Ma) and Jurassic (~170 Ma) age peaks similar to those obtained from the Caballos Formation (Fig. 5). These age populations are also similar to the zircon U—Pb ages obtained from the igneous and metamorphic rocks exposed in the Garzón massif (180–160 Ma and 1500–900 Ma), including sample 34054Gz (Figs. 5a and 8a) and published U—Pb ages of basement rocks (Bustamante et al., 2010; Rodríguez et al., 2018; Ibañez-Mejia et al., 2011). This interpretation is supported by the petrographic data, where the high content of subangular to subrounded monocrystalline quartz is likely associated with metamorphic and plutonic rocks (Fig. 8c).

A typical section of continental crust includes sedimentary and volcanic rocks at the top and plutonic and metamorphic rocks at depth (Garzanti, 2016). Currently, the Garzón massif mainly exposes high-grade metamorphic rocks with associated intrusive bodies (Fig. 1a). Considering the low-metamorphic and sedimentary lithics found in the Caballos Formation and the detrital zircon signature, we suggest that an upper crustal segment of the Garzón massif, which likely had lower-grade metamorphism but similar age signatures, acted as a source area together with less exposed high-grade metamorphic rocks of the Garzón massif. The presence of sedimentary lithics can be explained by the sources from the volcano-sedimentary strata from the Saldaña Formation, as suggested by the presence of Jurassic zircon ages.

Based on the provenance of the Caballos Formation, we interpret that the Garzón massif was exposed between 120 and 100 Ma (Fig. 9). The presence of a positive relief in the Garzón massif between 120 and 100 Ma can be related to the segmentation of the Andean extensional basins during this time and the absence of an integrated regional drainage network (León et al., 2023).

5.3. *Onset of contractional setting during the Late Cretaceous (100 to 80 Ma)*

The Villeta Group was deposited during the Cenomanian-Santonian. In stratigraphic sections 2 and 3, this unit is characterized by inner- to mid-shelf deposits in shallow marine environments (Table 2; Figs. 3 and 8b), suggesting basin-deepening. The studied area was likely part of a regional carbonate ramp developed in eastern Colombia between ~100 and 80 Ma (Sarmiento-Rojas, 2019). This depositional system includes the deposition of the La Luna Formation in the Middle Magdalena Basin and the Eastern Cordillera, a unit that has been correlated with the Villeta Group (Casadiego-Quintero and Ríos-Reyes, 2016; Guerrero et al., 2020a, 2020b; Rangel et al., 2000). Although we do not present detrital U—Pb zircon data from the Villeta Group, the petrographic data and ZFT detrital ages indicate that there were no major provenance changes in the Villeta Group with respect to the Caballos Formation. Therefore, we suggest that the Garzón massif may have also acted as source area a during the deposition of the Villeta Group. Following the marine sedimentation of the Villeta Group, the Oliní Group records the basin deepening during the Santonian-Campanian (Fig. 8b; see the

paleogeographic reconstruction from Sarmiento-Rojas, 2019).

The deposition of the Villeta Group overlaps with the Cretaceous cooling event (~100 and 85 Ma) in the Garzón massif (Fig. 6c). This sedimentary record and the associated cooling event occurred during a prolonged period that includes the regional transition from extension to contraction in the Colombian Andes (Bayona, 2018; Cardona et al., 2020; Zapata et al., 2019a).

In the UMB, internal discordances within the Villeta Group have been presented as evidence for the transition to contraction (Fig. S7) (Jaimes and de Freitas, 2006). The Late Cretaceous cooling record unraveled by the thermal history of the Garzón massif between ~100 and 85 Ma could be related to post-extension cooling, the onset of contraction, or a combination of both. Given the Albian-Cenomanian intraformational discordances in the Villeta Group, we propose that the Cretaceous cooling in the Garzón massif was associated with the onset of the contractional phase (Figs. 6c and 9). The apparent inconsistency related to the coeval basin deepening represented by the Oliní Group and the onset of contraction may be explained by a significant rise in the sea level (Barrio and Coffield, 1992; Hallam, 1984; Haq, 2014; Miller et al., 2004) combined with minor rock uplift within the basin, indicating that contraction began as localized and low magnitude events.

This Cretaceous cooling between ~100 and 85 Ma suggests that the Garzón massif had positive relief at least until ~85 Ma. Regional stratigraphy indicates that the Villeta Group was also deposited in the Putumayo Basin (Mora-Bohorquez et al., 2010); this sedimentary pattern may suggest a discontinuous topography in the Garzón massif, where some segments may have been covered by the Villeta Group while other basement blocks experienced uplift and erosion.

Bedrock ZFT cooling ages between 100 and 74 Ma have been documented in the Central Cordillera, on the western margin of the basin (Villamizar-Escalante et al., 2021). These data, together with the thermal history model of the Garzón massif presented here (Fig. 6c) suggest coeval exhumation in the western and eastern boundaries of the UMB during the Late Cretaceous, forming a broken foreland basin that implies the existence of intra-basin uplifts disconnected from the main orogenic front (del Papa et al., 2021; Horton et al., 2022; Strecker et al., 2011).

5.4. Eastern basement uplift and topographic growth in the Late Cretaceous (80 to 70 Ma)

After the deposition of the Santonian-Campanian Oliní Group, the deposition of the Maastrichtian (~72 Ma) La Tabla Formation in a sandy shelf transitional environment marked a major shift in the sedimentary systems (Table 2; Fig. 3).

La Tabla Formation sandstones are characterized by high quartz content (>70%), and low lithic content (~2%) (Figs. 4a and 8c). The dominant quartz-type is undulatory-monocrystalline, and the lithic fraction consists of sedimentary and low-grade metamorphic lithics, suggesting metamorphic and sedimentary rocks as the main source areas. The contribution of high-grade metamorphic rocks is also supported by the ratio between undulatory-monocrystalline and polycrystalline quartz in both samples (Fig. 4d).

Detrital zircon U—Pb age populations from the La Tabla Formation exhibit Proterozoic (2000–1000 Ma) age peaks. Populations between 1500 and 1000 Ma can be supplied from the Garzón massif, however, older ages require provenance from rocks exposed in the western segment of the Amazon craton, such as rocks from the Putumayo orogen, and the detrital signature of Paleozoic rocks exposed in the Macarena range (Figs. 5 and 8a) (Horton et al., 2010; Ibañez-Mejia et al., 2011; Pastor-Chacón et al., 2023). The distal position of the UMB may explain the lack of sedimentary sources from the Central Cordillera in the La Tabla Formation.

Since chemically unstable minerals are eliminated during prolonged weathering processes (León et al., 2023; Smyth et al., 2008), the quartz-rich composition of the La Tabla sandstones may also indicate high-weathering conditions and low relief in the source areas, during transport and/or at the deposition site. These source area characteristics are consistent with the incorporation of sediments derived from cratonic regions to the basin.

These provenance and stratigraphic observations from the La Tabla Formation suggest that the metamorphic and sedimentary rocks exposed in the Amazon craton were a source area for the UMB (Figs. 8 and 10). The absence of exhumation in the Garzón massif suggests the cease of rock uplift, which may have facilitated the arrival of sediment derived from eastern source areas (Fig. 6c). Moreover, seismic data from the south of the Upper Magdalena and Putumayo basins exhibit a continuous thickness of the preserved Paleogene sedimentary sequences, suggesting that these basins were connected at this time and that the Garzón massif was buried (Mora-Bohorquez et al., 2010; Saeid et al., 2017). Maastrichtian sedimentary successions are unconformably deposited on the Precambrian basement of the Macarena range (Fig. 1a) (Buchely et al., 2015), indicating that this basement block acted as a positive relief during the Late Cretaceous.

Two scenarios may explain the appearance of eastern cratonic source areas during the Late Cretaceous. The first is the continuation of broken foreland sedimentation, where after the initial exhumation of the Garzón massif between 100 and 80 Ma, deformation migrated eastward, deforming isolated basement blocks that are now in the Amazon craton (Moreno-López and Escalona, 2015; Pachón-Parra et al., 2020). The second is related to the eastward migration of source areas due to flexural basin subsidence generated by topographic loading in the Central Cordillera (e.g. Moreno-López and Escalona, 2015). These scenarios are schematized in Fig. 10; however, the provenance data do not resolve the tectonic mechanisms that allowed the appearance of eastern sources in the UMB.

5.5. Major western basement uplift and topographic growth in the Late Cretaceous (70 to 65 Ma)

The Maastrichtian-Paleocene Seca Formation marks a final shift in the source areas of the Cretaceous-Paleocene sedimentary systems in the UMB. The facies distribution described in section 1 (Table 2; Fig. 3) suggests that this unit was deposited in a coastal plain strongly influenced by fluvial processes under oxidizing conditions, as also suggested by the lithological and biostratigraphic data from previous studies (Bayona, 2018; Carvajal-Torres et al., 2022; Guerrero et al., 2000).

The sandstone of the Seca Formation is characterized by a significant increase in the lithic fraction (>70%) compared to the other Cretaceous units, which includes a high content of sedimentary lithics and the appearance of volcanic lithics (Figs. 4 and 8c). Detrital zircon U—Pb age populations include the appearance of Cretaceous (~82 Ma) and Jurassic (~187 Ma) peaks implying a decrease in Proterozoic ages compared to the Maastrichtian La Tabla and Aptian-Albian Caballos formations (Fig. 8). These provenance characteristics suggest that Mesozoic sedimentary and volcanic rocks constituted the primary source areas of the Seca Formation. This provenance signature is likely derived from the Cretaceous and Jurassic magmatic and volcano-sedimentary rocks exposed in the Central Cordillera (Figs. 1 and 8a) (Cardona et al., 2020; Duque-Trujillo et al., 2019; Leal-Mejía et al., 2019; Villagómez et al., 2011).

Stratigraphic and provenance constraints for the Seca Formation show a shift to continental sedimentation with western source areas (Fig. 8). This modification on the basin source areas can be explained by significant topographic growth in the western basin boundary and burial of the eastern basement highs. Topographic growth may have caused the development of fluvial continental depositional systems sourced from the Central Cordillera (Fig. 10). This major change was likely associated with the final stages of the Caribbean plateau collision, where substantial uplift and exhumation characterized the Central Cordillera (Cardona et al., 2020; George et al., 2021; Montes et al., 2019; Spikings et al., 2015; Zapata et al., 2021).

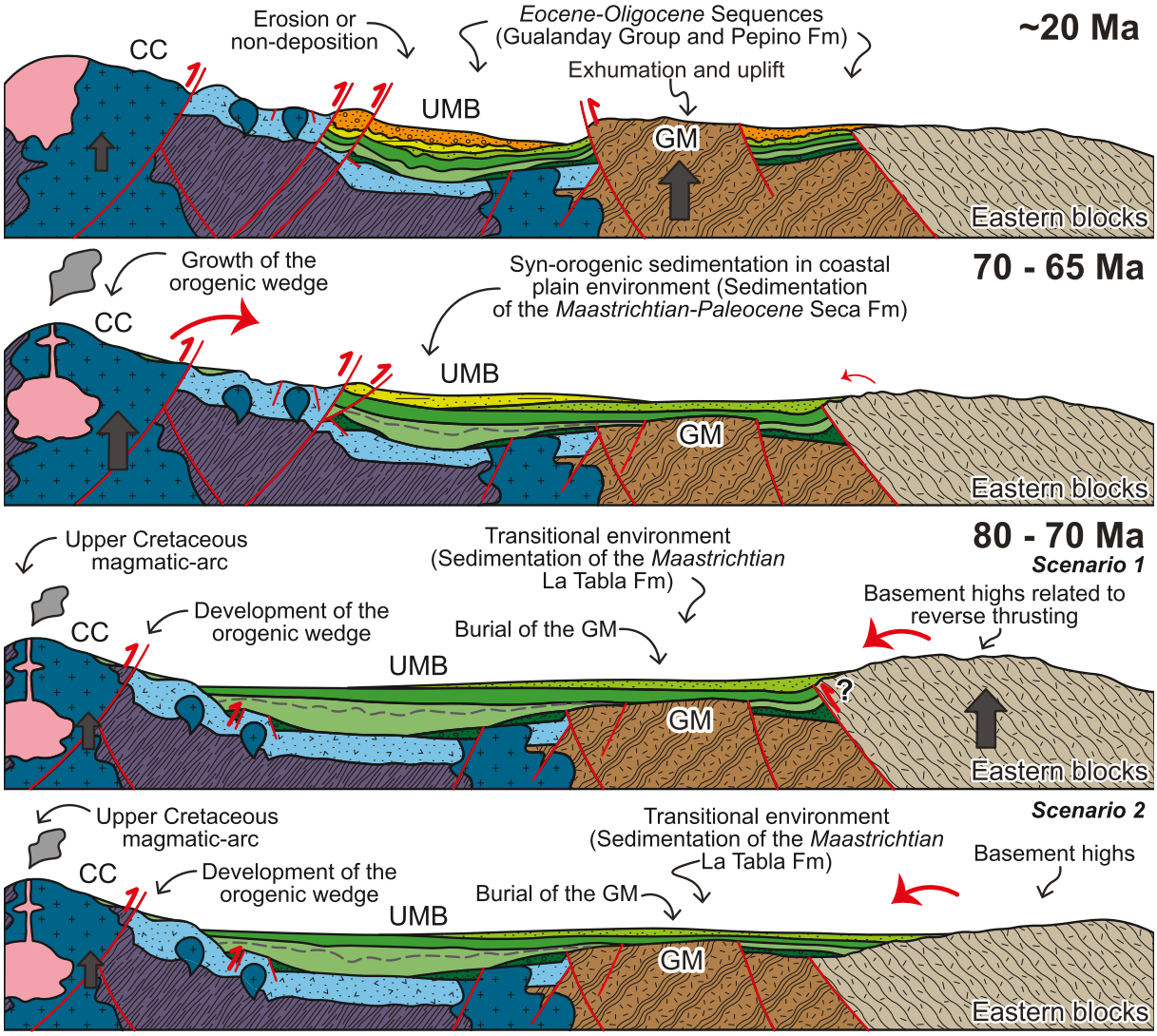

Fig. 10. Schematic model for the Late Cretaceous and the Miocene. Note that there are two scenarios between 80 and 70 Ma (see chapter 5.4). For detailed caption and legend see Fig. 9.

5.6. Cenozoic evolution in the UMB

After the Cretaceous tectonic phases recorded by the detrital and bedrock data, the Garzón massif block experienced slow burial and reheating until the final cooling phase at ~20 Ma (Fig. 6c), which could be associated with the major exhumation and uplift pulse in this block during the final phases of the Andean orogeny (Anderson et al., 2016; Pérez-Consuegra et al., 2021; Ramon and Rosero, 2006; Saeid et al., 2017; Van Der Wiel, 1991; Zapata et al., 2023).

In contrast, the Central Cordillera experienced slow cooling trends between the Oligocene - Early Miocene and constituted a continuous barrier at this time (Cardona et al., 2018; Echeverri et al., 2015; Zapata et al., 2023; Zapata et al., 2021). Our thermal history model suggests that this segment of the Garzón massif experienced a rapid cooling phase at 20 Ma (Fig. 6c), prior to the major uplift phases at ~12 and 6 Ma (Anderson et al., 2016; Saeid et al., 2017; Zapata et al., 2023). Coeval with the onset of exhumation in the Garzon massif, the UMB experienced an erosion or non-deposition period, resulting to the unconformity between the Eocene-Oligocene Gualanday Group and the Miocene Barzalosa Formation (Fig. 10) (de La Parra et al., 2019; Zapata et al., 2023).

6. Conclusions

A multi-technique source-to-sink analysis of the Cretaceous strata from the Upper Magdalena Basin (UMB) and the adjacent Garzón massif reveals a multi-phase evolution under contrasting paleogeographic and tectonic settings during the Cretaceous. Our results document Late Jurassic to Early Cretaceous exhumation likely related to Jurassic contraction and the onset of basement exhumation, followed by one major extensional phase and three contractional stages in the UMB during the Cretaceous. This model highlights how progressive extension led to the development of new depocenters and how contractional settings are characterized by disorganized basement uplift patterns and progressive topographic growth.

The detrital thermochronological ages from the Cretaceous strata suggest exhumation between ~160 and 120 Ma, which is probably related to the Late Jurassic deformation and the Early Cretaceous extension in the Garzón massif and other eastern blocks. This event was followed by a major extensional event between ~120 and 100 Ma coeval with the deposition of the Caballos Formation. During both extensional phases, the Garzón massif was exhumed and acted as a horst block limiting the basin to the east.

Between ~100 and 80 Ma, the transition to contractional settings is

evidenced by an increase in clastic supply, intrabasinal fault reactivation, and basement cooling in the Garzón massif. The accumulation of the La Tabla Formation between 80 and 70 Ma was coeval with the collision of the Caribbean plateau in the west and basement uplift in the Amazon craton. The development of topographic load during contraction may have promoted the subsidence and burial of the Garzón massif. Finally, during the deposition of the Seca Formation in continental environments, this contractional event prompted significant topographic growth and exhumation in the Central Cordillera. As a result, the Central Cordillera became the major source area of the UMB between 70 and 65 Ma. Finally, a major exhumation and uplift pulse is recorded in the Garzón massif at ~20 Ma and in the Miocene sedimentary sequences in the UMB.

Submission declaration and verification

Authors declare that this work has not been published previously.

CRediT authorship contribution statement

L. Calderon-Diaz: Conceptualization, Methodology, Investigation, Writing - original draft preparation, Visualization. **S. Zapata:** Conceptualization, Investigation, Validation, Resources, Writing - review & editing, Visualization, Supervision. **A. Cardona:** Conceptualization, Validation, Resources, Writing - review & editing, Visualization, Supervision. **M. Parra:** Resources, Writing – review & editing. **E.R. Sobel:** Resources, Writing - review & editing. **A.M. Patiño:** Investigation. **V. Valencia:** Resources. **J.S. Jaramillo-Rios:** Investigation. **J. Glodny:** Resources, Writing - review & editing.

Declaration of competing interest

The authors declare that they have no known competing financial interests or personal relationships that could have appeared to influence the work reported in this paper.

Data availability

All the data used in this manuscript can be found in the supporting information, and thermochronological and geochronological data are also stored in Geochron repository (http://www.geochron.org/dataset/html/geochron_dataset_2023_08_24_dfg2H).

Acknowledgements

We acknowledge the support of Minciencias and the Agencia Nacional de Hidrocarburos (ANH) for the project “Structural modeling and petrophysical characterization of the fractured crystalline basement reservoir analogs in the Upper Magdalena Valley, Colombia, ¿a new exploration opportunity? (CT 80740-152-2021). We also thank the Rosario University for their financial support through the starting fund. Colleagues from the EGEO research group at the National University of Colombia are acknowledged for their discussions and feedback. L. Calderon-Diaz thanks the American Association of Petroleum Geologists (AAPG) for the resources provided through the 2023 L. Austin Weeks Memorial Grant and the fellowship received from the Smithsonian Tropical Research Institute (STRI). Finally, we thank M. Bernet and S. George for their valuable feedback and comments, which significantly improved the manuscript.

Appendix A. Supplementary data

Supplementary data to this article can be found online at https://doi.org/10.1016/j.tecto.2024.230303.

References

Abbey, A.L., Wildman, M., Stevens Goddard, A.L., Murray, K.E., 2023. Thermal history modeling techniques and interpretation strategies: applications using QTQt. Geosphere 19 (2), 493–530.

Acosta, J., Velandia, F., Osorio, J., Lonergan, L., Mora, H., 2007. Strike-slip deformation within the Colombian Andes. Geol. Soc. Spec. Publ. 272 (1), 303–319. https://doi.org/10.1144/gsl.sp.2007.272.01.16.

Amaya-López, C., Restrepo Álvarez, J.J., Weber Scharff, M., Cuadros Jiménez, F.A., Botelho, N.F., Ibañez Mejía, M., Maya Sánchez, M., Pérez Parra, O.M., Ramírez Cárdenas, C., 2020. The Guaviare complex: new evidence of Mesoproterozoic (ca. 1.3 Ga) crust in the Colombian Amazonian Craton. Bol. Geol. 47, 5–34. https://doi.org/10.32685/0120-1425/boletingeo.47.2020.502.

Amaya-López, C., Weber Scharff, M., Ibáñez Mejía, M., Cuadros Jiménez, F.A., Restrepo Álvarez, J.J., Botelho, N.F., Maya Sánchez, M., Pérez Parra, O.M., Ramírez Cárdenas, C., 2021. San José de Guaviare Syenite, Colombia: Repeated Ediacaran intrusions in the northwestern Amazonian Craton. Bol. Geol. 48 (1), 49–79. https://doi.org/10.32685/0120-1425/bol.geol.48.1.2021.503.

Anderson, T.A., 1972. Paleogene nonmarine gualanday group, Neiva basin, Colombia, and regional development of the Colombian Andes. Geol. Soc. Am. Bull. 83 (8), 2423. https://doi.org/10.1130/0016-7606(1972)83[2423:pnggnb]2.0.co;2.

Anderson, V.J., Horton, B.K., Saylor, J.E., Mora, A., Tesón, E., Breecker, D.O., Ketcham, R.A., 2016. Andean topographic growth and basement uplift in southern Colombia: Implications for the evolution of the Magdalena, Orinoco, and Amazon river systems. Geosphere 12 (4), 1235–1256. https://doi.org/10.1130/ges01294.1.

Anderson, A.J., van Soest, M.C., Hodges, K.V., Hanchar, J.M., 2020. Helium diffusion in zircon: Effects of anisotropy and radiation damage revealed by laser depth profiling. Geochim. Cosmochim. Acta 274, 45–62. https://doi.org/10.1016/j.gca.2020.01.049.

Angiolini, L., Racheboeuf, P.R., Villarroel, C.A., Concha, A.E., 2021. Stratigraphy and brachiopod fauna of the Carboniferous El Imán Formation, Colombia. Spanish J. Palaeontol. 18 (2), 151. https://doi.org/10.7203/sjp.18.2.21641.

Ault, A.K., Guenthner, W.R., Moser, A.C., Miller, G.H., Refsnider, K.A., 2018. Zircon grain selection reveals (de)coupled metamictization, radiation damage, and he diffusivity. Chem. Geol. 490, 1–12. https://doi.org/10.1016/j.chemgeo.2018.04.023.

Ault, A.K., Gautheron, C., King, G.E., 2019. Innovations in (U–Th)/he, fission track, and trapped charge thermochronometry with applications to earthquakes, weathering, surface-mantle connections, and the growth and decay of mountains. Tectonics 38 (11), 3705–3739. https://doi.org/10.1029/2018tc005312.

Bajolet, F., Chardon, D., Rouby, D., Dall'Asta, M., Loparev, A., Couëffe, R., Roig, J.-Y., 2022. The sediment routing systems of Northern South America since 250 Ma. Earth Sci. Rev. 232 (104139), 104139 https://doi.org/10.1016/j.earscirev.2022.104139.

Barrio, C.A., Coffield, D.Q., 1992. Late cretaceous stratigraphy of the Upper Magdalena Basin in the Payandé-Chaparral segment (western Girardot Sub-Basin), Colombia. J. S. Am. Earth Sci. 5 (2), 123–139. https://doi.org/10.1016/0895-9811(92)90034-v.

Basu, A., Young, S.W., Suttener, L.J., James, W.C., Mack, G., 1975. Re-evaluation of the use of undulatory extinction and polycristallinity in detrital quartz for provenance interpretation. J. Sediment. Petrol. 4, 873–882.

Bayona, G., 2018. El inicio de la emergencia en los Andes del norte: una perspectiva a partir del registro tectónico-sedimentológico del Coniaciano al Paleoceno. Rev. de La Acad. Colombiana de Ciencias Exactas, Fisicas y Naturales 42 (165), 364. https://doi.org/10.18257/raccefyn.632.

Bayona, G., García, D., Mora, G., 1994. La Formación Saldaña: producto de la actividad de estratovolcanes continentales en un dominio de retroarco, en Etayo-Serna, F., ed., Estudios Geológicos del Valle Superior del Magdalena: Bogotá, Universidad Nacional de Colombia. Capítulo I 21.

Bayona, G., Rapalini, A., Costanzo-Alvarez, V., 2006. Paleomagnetism in Mesozoic rocks of the Northern Andes and its Implications in Mesozoic Tectonics of Northwestern South America. Earth Planets Space 58 (10), 1255–1272. https://doi.org/10.1186/bf03352621.

Bayona, G., Cardona, A., Jaramillo, C., Mora, A., Montes, C., Valencia, V., Ayala, C., Montenegro, O., Ibañez-Mejia, M., 2012. Early Paleogene magmatism in the northern Andes: Insights on the effects of Oceanic Plateau–continent convergence. Earth Planet. Sci. Lett. 331–332, 97–111. https://doi.org/10.1016/j.epsl.2012.03.015.

Bayona, G., Cardona, A., Jaramillo, C., Mora, A., Montes, C., Caballero, V., Mahecha, H., Lamus, F., Montenegro, O., Jimenez, G., Mesa, A., Valencia, V., 2013. Onset of fault reactivation in the Eastern Cordillera of Colombia and proximal Llanos Basin; response to Caribbean–South American convergence in early Palaeogene time. Geol. Soc. Spec. Publ. 377 (1), 285–314. https://doi.org/10.1144/sp377.5.

Bayona, G., Bustamante, C., Nova, G., Salazar-Franco, A.M., 2020. Jurassic evolution of the northwestern corner of Gondwana: Present knowledge and future challenges in studying Colombian Jurassic rocks. In: Gómez, J., Pinilla-Pachon, A.O. (Eds.), The Geology of Colombia, Volume 2 Mesozoic. Servicio Geológico Colombiano, 36. Publicaciones Geológicas Especiales, Bogotá, pp. 171–207. https://doi.org/10.32685/pub.esp.36.2019.05.

Bayona, G., Baquero, M., Ramírez, C., Tabares, M., Salazar, A.M., Nova, G., Duarte, E., Pardo, A., Plata, A., Jaramillo, C., Rodríguez, G., Caballero, V., Cardona, A., Montes, C., Gómez Marulanda, S., Cárdenas-Rozo, A.L., 2021. Unravelling the widening of the earliest Andean northern orogen: Maastrichtian to early Eocene intra-basinal deformation in the northern Eastern Cordillera of Colombia. Basin Res. 33 (1), 809–845. https://doi.org/10.1111/bre.12496.

Beltrán, N., Gallo, J., 1968. Guidebook to the Geology of the Neiva Sub-Basin, Upper Magdalena Basin (Southern Portion). Colombian Society of Petroleum Geologists and Geophysicists.
Bernet, M., 2009. A field-based estimate of the zircon fission-track closure temperature. Chem. Geol. 259 (3–4), 181–189. https://doi.org/10.1016/j.chemgeo.2008.10.043.
Bernet, M., Garver, J., 2005. Fission-track analysis of detrital zircon. Rev. Mineral. Geochem. 58 (1), 205–237. https://doi.org/10.2138/rmg.2005.58.8.
Bernet, M., Brandon, M., Garver, J., Balestieri, M.L., Ventura, B., Zattin, M., 2009. Exhuming the Alps through time: clues from detrital zircon fission-track thermochronology. Basin Res. 21 (6), 781–798. https://doi.org/10.1111/j.1365-2117.2009.00400.x.
Blanco-Quintero, I.F., García-Casco, A., Toro, L.M., Moreno, M., Ruiz, E.C., Vinasco, C.J., Cardona, A., Lázaro, C., Morata, D., 2014. Late Jurassic terrane collision in the northwestern margin of Gondwana (Cajamarca complex, eastern flank of the Central Cordillera, Colombia). Int. Geol. Rev. 56 (15), 1852–1872. https://doi.org/10.1080/00206814.2014.963710.
Borrero, C., Sarmiento, G., Gomez-Gonzalez, C., Gutiérrez-Marco, J., 2007. Los conodontos de la Formación el Hígado y su contribución al conocimiento del metamorfismo y la paleogeografía del Ordovícico en la Cordillera Central colombiana. Bolet. de Ciencias de La Tierra 29 (2), 39–46.
Brandon, M.T., 1996. Probability density plot for fission-track grain-age samples. Radiat. Meas. 26 (5), 663–676.
Brandon, M.T., Roden-Tice, M.K., Garver, J.I., 1998. Late Cenozoic exhumation of the Cascadia accretionary wedge in the Olympic Mountains, Northwest Washington State. Geol. Soc. Am. Bull. 110 (8), 985–1009. https://doi.org/10.1130/0016-7606(1998)110<0985:lceotc>2.3.co;2.
Bridge, J.S., 2003. Rivers and Floodplains: Forms, Processes, and Sedimentary Record. John Wiley & Sons.
Brown, R.W., Beucher, R., Roper, S., Persano, C., Stuart, F., Fitzgerald, P., 2013. Natural age dispersion arising from the analysis of broken crystals. Part I: Theoretical basis and implications for the apatite (U–Th)/he thermochronometer. Geochim. Cosmochim. Acta 122, 478–497. https://doi.org/10.1016/j.gca.2013.05.041.
Brune, S., Heine, C., Clift, P.D., Pérez-Gussinyé, M., 2017. Rifted margin architecture and crustal rheology: reviewing Iberia-Newfoundland, central South Atlantic, and South China Sea. Mar. Petrol. Geol. 79, 257–281.
Brune, S., Kolawole, F., Olive, J.-A., Stamps, D.S., Buck, W.R., Buiter, S.J.H., Furman, T., Shillington, D.J., 2023. Geodynamics of continental rift initiation and evolution. Nat. Rev. Earth & Environ. 4 (4), 235–253. https://doi.org/10.1038/s43017-023-00391-3.
Buchely, F., Gomez, L., Buitrago, J., Cristancho, A., Moreno-Sánchez, M., Gómez, L., Aranzazu, J.M., Castelblanco, E., Tovar, A., Ramos, J., Ojeda, C., Facio-Lince, I., Quiñones, C., 2015. Geología de la plancha 326 - Vista Hermosa. Escala 1, 100.000. 5–48.
Burnham, A.K., Sweeney, J.J., 1989. A chemical kinetic model of vitrinite maturation and reflectance. Geochim. Cosmochim. Acta 53 (10), 2649–2657.
Bustamante, C., Cardona, A., Bayona, G., Mora, A., Valencia, V., Gehrels, G., Vervoort, J., 2010. U-Pb LA-ICP-MS Geochronology and Regional Correlation of Middle Jurassic Intrusive Rocks from the Upper Magdalena Valley and Central Cordillera, Southern Colombia. Rev. Boletín de Geol. 32 (2), 93–109. http://www.scielo.org.co/scielo.php?pid=S0120-02832010000200007&script=sci_arttext&tlng=en.
Bustamante, C., Archanjo, C.J., Cardona, A., Vervoort, J.D., 2016. Late Jurassic to early cretaceous plutonism in the Colombian Andes: A record of long-term arc maturity. Geol. Soc. Am. Bull. 128 (11−12), 1762–1779. https://doi.org/10.1130/b31307.1.
Bustamante, C., Archanjo, C.J., Cardona, A., Bustamante, A., Valencia, V.A., 2017. U-Pb ages and hf isotopes in zircons from parautochthonous Mesozoic terranes in the western margin of pangea: Implications for the Terrane configurations in the northern Andes. J. Geol. 125 (5), 487–500. https://doi.org/10.1086/693014.
Butler, K., Schamel, S., 1988. Structure along the eastern margin of the central Cordillera, upper Magdalena Valley, Colombia. J. S. Am. Earth Sci. 1 (1), 109–120. https://doi.org/10.1016/0895-9811(88)90019-3.
Caracciolo, L., 2020. Sediment generation and sediment routing systems from a quantitative provenance analysis perspective: Review, application and future development. Earth Sci. Rev. 209 (103226), 103226 https://doi.org/10.1016/j.earscirev.2020.103226.
Cardona, A., Montes, C., Ayala, C., Bustamante, C., Hoyos, N., Montenegro, O., Ojeda, C., Niño, H., Ramirez, V., Valencia, V., Rincón, D., Vervoort, J., Zapata, S., 2012. From arc-continent collision to continuous convergence, clues from Paleogene conglomerates along the southern Caribbean–South America plate boundary. Tectonophysics 580, 58–87. https://doi.org/10.1016/j.tecto.2012.08.039.
Cardona, A., León, S., Jaramillo, J.S., Montes, C., Valencia, V., Vanegas, J., Bustamante, C., Echeverri, S., 2018. The Paleogene arcs of the northern Andes of Colombia and Panama: Insights on plate kinematic implications from new and existing geochemical, geochronological and isotopic data. Tectonophysics 749 (88–109). S0040195118303743.
Cardona, A., León, S., Jaramillo, J.S., Valencia, V., Zapata, S., Pardo-Trujillo, A., Schmitt, A.K., Mejía, D., Arenas, J.C., 2020. Cretaceous record from a Mariana– to an Andean–type margin in the Central Cordillera of the Colombian Andes. In: Gómez, J., Pinilla-Pachon, A.O. (Eds.), The Geology of Colombia, Volume 2 Mesozoic. Servicio Geológico Colombiano, 36. Publicaciones Geológicas Especiales, Bogotá, pp. 335–373. https://doi.org/10.32685/pub.esp.36.2019.10.
Carlson, W.D., Donelick, R.A., Ketcham, R.A., 1999. Variability of apatite fission-track annealing kinetics: I. Experimental results. Am. Mineral. 84 (9), 1213–1223.
Carvajal-Torres, J., Catuneanu, O., Mora, A., Caballero, V., Reyes, M., 2022. First-order stratigraphic boundaries of the Late Cretaceous–Paleogene retroarc foreland basin in Colombia. Front. Earth Sci. 10 https://doi.org/10.3389/feart.2022.876140.
Carvalho, M.R., Jaramillo, C., de la Parra, F., Caballero-Rodríguez, D., Herrera, F., Wing, S., Turner, B.L., D'Apolito, C., Romero-Báez, M., Narváez, P., Martínez, C., Gutierrez, M., Labandeira, C., Bayona, G., Rueda, M., Paez-Reyes, M., Cárdenas, D., Duque, Á., Crowley, J.L., Silvestro, D., 2021. Extinction at the end-cretaceous and the origin of modern neotropical rainforests. Science (New York, N.Y.) vol. 372 (6537), 63–68. https://doi.org/10.1126/science.abf1969.
Casadiego-Quintero, E., Ríos-Reyes, C.A., 2016. Lithofacies analysis and depositional environment of the Galembo Member of La Luna Formation. Tecnol. y Futuro 6 (4), 37–56.
Chang, Z., Vervoort, J.D., McClelland, W.C., Knaack, C., 2006. U-Pb dating of zircon by LA-ICP-MS. Geochem. Geophys. Geosyst. 7 (5).
Chen, W.-H., Yan, Y., Carter, A., Huang, C.-Y., Yumul Jr., G.P., Dimalanta, C.B., Gabo-Ratio, J.A.S., Wang, M.-H., Chen, D., Shan, Y., Zhang, X.-C., Liu, W., 2021. Stratigraphy and provenance of the Paleogene syn-rift sediments in Central-Southern Palawan: Paleogeographic significance for the South China margin. Tectonics 40 (9). https://doi.org/10.1029/2021tc006753.
Cloetingh, S., Burov, E., Matenco, L., Beekman, F., Roure, F., Ziegler, P.A., 2013. The Moho in extensional tectonic settings: Insights from thermo-mechanical models. Tectonophysics 609, 558–604. https://doi.org/10.1016/j.tecto.2013.06.010.
Coffey, K.T., Ingersoll, R.V., Schmitt, A.K., 2019. Stratigraphy, provenance, and tectonic significance of the Punchbowl block, San Gabriel Mountains, California, USA. Geosphere 15 (2), 479–501. https://doi.org/10.1130/ges02025.1.
Collinson, J., Mountney, N.P., Thompson, D., 2006. Sedimentary structures (third edition). In: Encyclopedia of Earth Sciences Series. https://doi.org/10.1038/208315b0.
Cooper, M.A., Addison, F.T., Alvarez, R., Coral, M., Graham, R.H., Hayward, A.B., Howe, S., Martinez, J., Naar, J., Peñas, R., Pulham, A.J., Taborda, A., 1995. Basin development and tectonic history of the Llanos Basin, Eastern Cordillera, and Middle Magdalena Valley, Colombia. Am. Assoc. Pet. Geol. Bull. 79 (10), 1421–1443.
Coutts, D.S., Matthews, W.A., Hubbard, S.M., 2019. Assessment of widely used methods to derive depositional ages from detrital zircon populations. Geosci. Front. 10 (4), 1421–1435. https://doi.org/10.1016/j.gsf.2018.11.002.
de La Parra, F., Pinzon, D., Rodriguez, G., Bedoya, O., Benson, R., 2019. Lacustrine systems in the early Miocene of Northern South America—evidence from the upper Magdalena Valley, Colombia. Palaios 34, 490–505. https://doi.org/10.2110/palo.2019.025.
De Porta, J., 1966. Geologia del extremo S del Valle Medio del Magdalena entre Honda y Guataquí (Colombia). Boletín de Geol. 21 https://doi.org/10.18273/revbol.
DeCelles, Peter G., Giles, K.A., 1996. Foreland basin systems. Basin Res. 8 (2), 105–123. https://doi.org/10.1046/j.1365-2117.1996.01491.x.
DeCelles, Peter G., Ducea, M.N., Kapp, P., Zandt, G., 2009. Cyclicity in Cordilleran orogenic systems. Nat. Geosci. 2 (4), 251–257. https://doi.org/10.1038/ngeo469.
DeCelles, P.G., Carrapa, B., Horton, B.K., Gehrels, G.E., 2011. Cenozoic foreland basin system in the Central Andes of northwestern Argentina: Implications for Andean geodynamics and modes of deformation: Andean Foreland Basin. Tectonics 30 (6). https://doi.org/10.1029/2011tc002948.
Decou, A., von Eynatten, H., Dunkl, I., Frei, D., Wörner, G., 2013. Late Eocene to Early Miocene Andean uplift inferred from detrital zircon fission track and U–Pb dating of Cenozoic forearc sediments (15–18°S). J. S. Am. Earth Sci. 45, 6–23. https://doi.org/10.1016/j.jsames.2013.02.003.
del Papa, C., Payrola, P., Pingel, H., Hongn, F., Do Campo, M., Sobel, E.R., Lapiana, A., Cottle, J., Glodny, J., Strecker, M.R., 2021. Stratigraphic response to fragmentation of the Miocene Andean foreland basin, NW Argentina. Basin Res. 33 (6), 2914–2937. https://doi.org/10.1111/bre.12589.
Destro, N., 1995. Release fault: A variety of cross fault in linked extensional fault systems, in the Sergipe-Alagoas Basin, NE Brazil. J. Struct. Geol. 17 (5), 615–629. https://doi.org/10.1016/0191-8141(94)00088-h.
Dickinson, W.R., 1985. Interpreting provenance relations from detrital modes of sandstones. In: Provenance of Arenites. Springer, Netherlands, pp. 333–361.
Donelick, R.A., Ketcham, R.A., Carlson, W.D., 1999. Variability of apatite fission-track annealing kinetics: II. Crystallographic orientation effects. Am. Mineral. 84 (9), 1224–1234.
Dong, Y., Zhang, G., Neubauer, F., Liu, X., Genser, J., Hauzenberger, C., 2011. Tectonic evolution of the Qinling orogen, China: Review and synthesis. J. Asian Earth Sci. 41 (3), 213–237. https://doi.org/10.1016/j.jseaes.2011.03.002.
Duarte, E., Cardona, A., Lopera, S., Valencia, V., Estupiñan, H., 2018. Provenance and diagenesis from two stratigraphic sections of the lower cretaceous Caballos formation in the upper Magdalena valley: Geological and reservoir quality implications. CTyF - Ciencia. Tecnol. y Futuro 8 (1), 5–29. https://doi.org/10.29047/01225383.88.
Dunham, R.J., 1962. Classification of carbonate rocks according to depositional textures.
Duque-Trujillo, J., Bustamante, C., Solari, L., Gómez-Mafla, Á., Toro-Villegas, G., Hoyos, S., 2019. Reviewing the Antioquia batholith and satellite bodies: a record of late cretaceous to Eocene syn-to post-collisional arc magmatism in the Central Cordillera of Colombia. Andean Geol. 46 (1), 82–101.
Echeverri, S., Cardona, A., Pardo, A., Monsalve, G., Valencia, V.A., Borrero, C., Rosero, S., López, S., 2015. Regional provenance from southwestern Colombia fore-arc and intra-arc basins: implications for Middle to late Miocene orogeny in the Northern Andes. Terra Nova 27 (5), 356–363. https://doi.org/10.1111/ter.12167.
Espitia, W., Cortés, M., Beltrán, W., Higuera Díaz, I.C., Arias, J., 2022. Structural styles of the Upper. In: Andean Structural Styles. Elsevier, Magdalena valley, Northern Andes, Colombia: Case Studies, pp. 139–148.
Etayo-Serna, F., Carrillo, G., 1996. Bioestratigrafía del cretácico mediante macrofósiles en la sección el Ocal. Valle Superior del Magdalena. Geología Colombiana, Colombia.

Farley, K.A., 2002. (U-Th)/he dating: Techniques, calibrations, and applications. Rev. Mineral. Geochem. 47 (1), 819–844. https://doi.org/10.2138/rmg.2002.47.18.
Farley, K.A., Wolf, R.A., Silver, L.T., 1996. The effects of long alpha-stopping distances on (U-Th)/he ages. Geochim. Cosmochim. Acta 60 (21), 4223–4229. https://doi.org/10.1016/s0016-7037(96)00193-7.
Fleischer, R.L., Price, P.B., Walker, R.M., 1975. Nuclear Tracks in Solids: Principles and Applications. Berkeley.
Flood, R.D., Hiscott, R.N., Aksu, A.E., 2009. Morphology and evolution of an anastomosed channel network where saline underflow enters the Black Sea. Sedimentology 56 (3), 807–839. https://doi.org/10.1111/j.1365-3091.2008.00998.x.
Flowers, Rebecca M., 2009. Exploiting radiation damage control on apatite (U–Th)/he dates in cratonic regions. Earth Planet. Sci. Lett. 277 (1–2), 148–155. https://doi.org/10.1016/j.epsl.2008.10.005.
Flowers, R.M., Zeitler, P.K., Danišík, M., Reiners, P.W., Gautheron, C., Ketcham, R.A., Metcalf, J.R., Stockli, D.F., Enkelmann, E., Brown, R.W., 2023. (U-Th)/he chronology: part 1. Data, uncertainty, and reporting. Geol. Soc. Am. Bull. 135 (1–2), 104–136. https://doi.org/10.1130/b36266.1.
Folk, R., 1980. Petrology of the Sedimentary Rocks, 190. Hemphill Publishing Company. https://doi.org/10.1016/0169-555x(91)90027-8.
Franco, R., Mojica, J., 1990. Estructura y Evolucion Tectonlca del Valle Medio y Superior del Magdalena, Colombia. Geolo. Colombiana 17, 41–64.
Galbraith, R.F., 2005. Statistics for Fission Track Analysis. CRC Press.
Galbraith, R.F., Laslett, G.M., 1993. Statistical models for mixed fission track ages. In: Nuclear Tracks and Radiation Measurements (Oxford, England : 1993), 21(4), pp. 459–470. https://doi.org/10.1016/1359-0189(93)90185-c.
Gallagher, K., 2012. Transdimensional inverse thermal history modeling for quantitative thermochronology: Transdimensional Inverse thermal history. J. Geophys. Res. 117 (B2) https://doi.org/10.1029/2011jb008825.
García-Chinchina, D., 2018. Petrogênese e Evolução Tectônica de Rochas Graníticas da Região de Garzón, Cordilheira Oriental da Colômbia (Doctoral dissertation,. Universidade De São Paulo, Instituto De Geociências.
Garver, J.I., Reiners, P.W., Walker, L.J., Ramage, J.M., Perry, S.E., 2005. Implications for timing of Andean uplift from thermal resetting of radiation-damaged zircon in the cordillera huayhuash, northern Peru. J. Geol. 113 (2), 117–138. https://doi.org/10.1086/427664.
Garzanti, E., 2016. From static to dynamic provenance analysis—Sedimentary petrology upgraded. Sediment. Geol. 336, 3–13. https://doi.org/10.1016/j.sedgeo.2015.07.010.
Garzanti, E., Vezzoli, G., 2003. A classification of metamorphic grains in sands based on their composition and grade. J. Sediment. Res. 73 (5), 830–837. https://doi.org/10.1306/012203730830.
Garzanti, E., Limonta, M., Vezzoli, G., An, W., Wang, J., Hu, X., 2018. Petrology and multimineral fingerprinting of modern sand generated from a dissected magmatic arc (Lhasa River, Tibet). In: Tectonics, Sedimentary Basins, and Provenance: A Celebration of the Career of William R. Dickinson. Geological Society of America.
Gautheron, C., Hueck, M., Ternois, S., Heller, B., Schwartz, S., Sarda, P., Tassan-Got, L., 2022. Investigating the shallow to mid-depth (>100–300 °C) continental crust evolution with (U-Th)/he thermochronology: A review. Minerals (Basel, Switzerland) 12 (5), 563. https://doi.org/10.3390/min12050563.
Gehrels, G.E., Valencia, V.A., Ruiz, J., 2008. Enhanced precision, accuracy, efficiency, and spatial resolution of U-Pb ages by laser ablation-multicollector-inductively coupled plasma-mass spectrometry. Geochem. Geophys. Geosyst. G(3), 9(3). https://doi.org/10.1029/2007gc001805.
George, S.W., Horton, B.K., Jackson, L.J., Moreno, F., Carlotto, V., Garzione, C.N., 2019. Sediment provenance variations during contrasting Mesozoic-early Cenozoic tectonic regimes of the northern Peruvian Andes and Santiago-Marañón foreland basin. In: Andean Tectonics. Elsevier, pp. 269–296.
George, S.W.M., Horton, B.K., Vallejo, C., Jackson, L.J., Gutierrez, E.G., 2021. Did accretion of the Caribbean oceanic plateau drive rapid crustal thickening in the northern Andes? Geology 49 (8), 936–940. https://doi.org/10.1130/g48509.1.
Gérard, B., Robert, X., Grujic, D., Gautheron, C., Audin, L., Bernet, M., Balvay, M., 2022. Zircon (U-Th)/he closure temperature lower than apatite thermochronometric systems: Reconciliation of a paradox. Minerals (Basel, Switzerland) 12 (2), 145. https://doi.org/10.3390/min12020145.
Girault, I., Basile, C., Bernet, M., Paquette, J.-L., Heuret, A., Loncke, L., Poetisi, E., Balvay, M., 2023. Thermochronology and U–Pb dating of detrital zircons from the Demerara Plateau (French Guiana-Suriname): Implications for the provenance of the Early Cretaceous syn-rift sedimentation. Basin Res. 35 (4), 1386–1406. https://doi.org/10.1111/bre.12758.
Gleadow, A.J.W., Duddy, I.R., 1981. A natural long-term track annealing experiment for apatite. Nucl. Tracks Radiat. Meas. 5 (1–2), 169–174. https://doi.org/10.1016/0191-278x(81)90039-1.
Gómez, E., Jordan, T.E., Allmendinger, R.W., Hegarty, K., Kelley, S., Heizler, M., 2003. Controls on architecture of the late cretaceous to Cenozoic southern Middle Magdalena Valley Basin, Colombia. Geol. Soc. Am. Bull. 115, 131–147. https://doi.org/10.1130/0016-7606(2003)115<0131:coaotl>2.0.co;2.
Gómez, E., Jordan, T.E., Allmendinger, R.W., Hegarty, K., Kelley, S., 2005. Syntectonic Cenozoic sedimentation in the northern middle Magdalena Valley Basin of Colombia and implications for exhumation of the Northern Andes. Geol. Soc. Am. Bull. 117 (5), 547. https://doi.org/10.1130/b25454.1.
Gómez, J., Montes, N.E., compiladores, 2020. Mapa Geológico de Colombia en Relieve 2020. Escala 1:1 000 000. Servicio Geológico Colombiano, 2 hojas. Bogotá. https://www2.sgc.gov.co/MGC/Paginas/mgc_1M2020.aspx.
Green, P.F., 1981. A new look at statistics in fission-track dating. Nuclear Track. 5 (1–2), 77–86.
Guenthner, W.R., Reiners, P.W., Ketcham, R.A., Nasdala, L., Giester, G., 2013. Helium diffusion in natural zircon: Radiation damage, anisotropy, and the interpretation of zircon (U-Th)/he thermochronology. Am. J. Sci. 313 (3), 145–198. https://doi.org/10.2475/03.2013.01.
Guerrero, J., Sarmiento, G., Narrete, R., 2000. The Stratigraphy of the W Side of the cretaceous Colombian Basin in the Upper Magdalena Valley. Reevaluation of selected areas and Type Localities Including Aipe, Guaduas, Ortega, and Piedras. Geolo. Colombiana 25, 45–110. http://www.revistas.unal.edu.co/index.php/geocol/article/view/31536.
Guerrero, J., Mejía-Molina, A., Osorno, J., 2020a. Detrital U–Pb provenance, mineralogy, and geochemistry of the Cretaceous Colombian back–arc basin. In: Gómez, J., Pinilla-Pachon, A.O. (Eds.), The Geology of Colombia, Volume 2 Mesozoic. Servicio Geológico Colombiano, 36. Publicaciones Geológicas Especiales, Bogotá, pp. 261–297. https://doi.org/10.32685/pub.esp.36.2019.08.
Guerrero, J., Mejía-Molina, A., Osorno, J., 2020b. Biomicrite, marlstone, and shale properties: Exploration of nonconventional hydrocarbons in the Cretaceous Colombian back– arc basin. In: Gómez, J., Pinilla-Pachon, A.O. (Eds.), The Geology of Colombia, Volume 2 Mesozoic. Servicio Geológico Colombiano, 36. Publicaciones Geológicas Especiales, Bogotá, pp. 299–333. https://doi.org/10.32685/pub.esp.36.2019.09.
Guerrero, J., Montes, L., Jaillard, E., Kammer, A., 2021. Seismic interpretation of the cretaceous unconformities and sequences in theMiddle Magdalena Valley and the western margin of the Eastern Cordillera. Géosci.-Sci. de La Planète 535, 155–172.
Hallam, A., 1984. Pre-Quaternary Sea-level changes. Annu. Rev. Earth Planet. Sci. 12 (1), 205–243. https://doi.org/10.1146/annurev.ea.12.050184.001225.
Haq, B.U., 2014. Cretaceous eustasy revisited. Glob. Planet. Chang. 113, 44–58. https://doi.org/10.1016/j.gloplacha.2013.12.007.
Harley, S.L., Kelly, N.M., 2007. Zircon tiny but timely. Elements (Quebec, Quebec) 3 (1), 13–18. https://doi.org/10.2113/gselements.3.1.13.
Harrington, H., Kay, M., 1951. Cambrian and Ordovician Faunas of Eastern Colombia. Source. J. Paleontol. 25 (5), 655–668.
Heermance, R.V., Chen, J., Burbank, D.W., Miao, J., 2008. Temporal constraints and pulsed late Cenozoic deformation during the structural disruption of the active Kashi foreland, Northwest China: Tian-Shan foreland deformation rates. Tectonics 27 (6). https://doi.org/10.1029/2007tc002226.
Horn, B.L.D., Goldberg, K., Schultz, C.L., 2017. Interpretation of massive sandstones in ephemeral fluvial settings: A case study from the Upper Candelária Sequence (Upper Triassic, Paraná Basin, Brazil). J. S. Am. Earth Sci. 81, 108–121. https://doi.org/10.1016/j.jsames.2017.10.009.
Horton, B.K., 2018. Tectonic regimes of the central and southern Andes: responses to variations in plate coupling during subduction. Tectonics 37 (2), 402–429. https://doi.org/10.1002/2017tc004624.
Horton, B.K., Saylor, J.E., Nie, J., Mora, A., Parra, M., Reyes-Harker, A., Stockli, D.F., 2010. Linking sedimentation in the northern Andes to basement configuration, Mesozoic extension, and Cenozoic shortening: evidence from detrital zircon U-Pb ages, Eastern Cordillera, Colombia. Geol. Soc. Am. Bull. 122 (9–10), 1423–1442. https://doi.org/10.1130/b30118.1.
Horton, B.K., Anderson, V.J., Caballero, V., Saylor, J.E., Nie, J., Parra, M., Mora, A., 2015. Application of detrital zircon U-Pb geochronology to surface and subsurface correlations of provenance, paleodrainage, and tectonics of the Middle Magdalena Valley Basin of Colombia. Geosphere 11 (6), 1790–1811. https://doi.org/10.1130/ges01251.1.
Horton, B.K., Capaldi, T.N., Mackaman-Lofland, C., Perez, N.D., Bush, M.A., Fuentes, F., Constenius, K.N., 2022. Broken foreland basins and the influence of subduction dynamics, tectonic inheritance, and mechanical triggers. Earth Sci. Rev. 234 (104193), 104193 https://doi.org/10.1016/j.earscirev.2022.104193.
Huismans, R.S., Podladchikov, Y.Y., Cloetingh, S., 2001. Transition from passive to active rifting: Relative importance of asthenospheric doming and passive extension of the lithosphere. J. Geophys. Res. Solid Earth 106 (B6), 11271–11291.
Ibañez-Mejia, M., Cordani, U.G., 2020. Zircon U–Pb geochronology and Hf–Nd–O isotope geochemistry of the Paleo– to Mesoproterozoic basement in the westernmost Guiana Shield. In: Gómez, J., Mateus-Zabala, D. (Eds.), The Geology of Colombia, Volume 1 Proterozoic – Paleozoic. Servicio Geológico Colombiano, 35. Publicaciones Geológicas Especiales, Bogotá, pp. 65–90. https://doi.org/10.32685/pub.esp.35.2019.04.
Ibañez-Mejia, M., Ruiz, J., Valencia, V.A., Cardona, A., Gehrels, G.E., Mora, A.R., 2011. The Putumayo Orogen of Amazonia and its implications for Rodinia reconstructions: New U–Pb geochronological insights into the Proterozoic tectonic evolution of northwestern South America. Precambrian Res. 191 (1–2), 58–77. https://doi.org/10.1016/j.precamres.2011.09.005.
Ibañez-Mejia, M., Pullen, A., Arenstein, J., Gehrels, G.E., Valley, J., Ducea, M.N., Mora, A.R., Pecha, M., Ruiz, J., 2015. Unraveling crustal growth and reworking processes in complex zircons from orogenic lower-crust: the Proterozoic Putumayo Orogen of Amazonia. Precambrian Res. 267, 285–310. https://doi.org/10.1016/j.precamres.2015.06.014.
Jaimes, E., de Freitas, M., 2006. An Albian–Cenomanian unconformity in the northern Andes: Evidence and tectonic significance. J. S. Am. Earth Sci. 21 (4), 466–492. https://doi.org/10.1016/j.jsames.2006.07.011.
Jaramillo, C., Yepes, O., Etayo-Serna, F., 1994. Palinoestratigrafía del Grupo Oliní (Coniaciano-Campaniano), Valle Superior del Magdalena. Estudios Geologicos del Valle Superior del Magdalena, Colombia.
Jaramillo, J.S., Cardona, A., León, S., Valencia, V., Vinasco, C., 2017. Geochemistry and geochronology from cretaceous magmatic and sedimentary rocks at 6°35′ N, western flank of the Central cordillera (Colombian Andes): Magmatic record of arc growth and collision. J. S. Am. Earth Sci. 76, 460–481. https://doi.org/10.1016/j.jsames.2017.04.012.

Jaramillo, J.S., Zapata, S., Carvalho, M., Cardona, A., Jaramillo, C., Crowley, J.L., Bayona, G., Caballero-Rodriguez, D., 2022. Diverse magmatic evolutionary trends of the Northern Andes unraveled by Paleocene to early Eocene detrital zircon geochemistry. Geochem. Geophys. Geosyst. 23 (9) e2021GC010113.

Johnson, J.E., Flowers, R.M., Baird, G.B., Mahan, K.H., 2017. "Inverted" zircon and apatite (U–Th)/he dates from the Front Range, Colorado: High-damage zircon as a low-temperature (<50 °C) thermochronometer. Earth Planet. Sci. Lett. 466, 80–90. https://doi.org/10.1016/j.epsl.2017.03.002.

Julivert, M., 1968. Lexique Stratigraphique International. Amerique Latine, Colombie (premiere partie)-Precambrien, Paleozoique, Mesozoique et intrusions d'age Mesozoique-Tertiaire. Centre Nat. Rech. Sci 5 (4a), 1–651.

Ketcham, R.A., Carter, A., Donelick, R.A., Barbarand, J., Hurford, A.J., 2007. Improved modeling of fission-track annealing in apatite. American Mineral. 92 (5–6), 799–810. https://doi.org/10.2138/am.2007.2281.

Kohn, B., Chung, L., Gleadow, A., 2019. Fission-track analysis: Field collection, sample preparation and data acquisition. In: Fission-Track Thermochronology and its Application to Geolog. Springer International Publishing, pp. 25–48.

Kumar, R., Suresh, N., Sangode, S.J., Kumaravel, V., 2007. Evolution of the Quaternary alluvial fan system in the Himalayan foreland basin: Implications for tectonic and climatic decoupling. Quat. Int. 159 (1), 6–20. https://doi.org/10.1016/j.quaint.2006.08.010.

Leal-Mejía, H., Shaw, R.P., Melgarejo, I., Draper, J.C., 2019. Spatial-Temporal Migration of Granitoid Magmatism and the Phanerozoic Tectono-Magmatic Evolution of the Colombian Andes. Geology and Tectonics of Northwestern South America. The Pacific-Caribbean-Andean Junction, pp. 253–410.

León, S., Cardona, A., Mejía, D., Botello, G.E., Villa, V., Collo, G., Valencia, V., Zapata, S., Avellaneda-Jiménez, D.S., 2019. Source area evolution and thermal record of an early cretaceous back-arc basin along the northwesternmost Colombian Andes. J. S. Am. Earth Sci. 94 (102229), 102229 https://doi.org/10.1016/j.jsames.2019.102229.

León, Santiago, Jiménez-Rodríguez, S., Piraquive, A., Florez-Amaya, S., Muñoz-Rocha, J., Peña-Urueña, M.L., Bonilla, A., Lince, I.F., Contreras-Fayad, D., Jiménez, C., 2023. Sediment provenance signal of the discontinuous retroarc topography in the northern Andes during the early cretaceous. Terra Nova. https://doi.org/10.1111/ter.12668.

Li, L., Najman, Y., Dupont-Nivet, G., Parra, M., Roperch, P., Kaya, M., Meijer, N., Osullivan, P., Jepson, G., Aminov, J., 2022. Mesozoic Cenozoic Multistage Tectonic Evolution of the Pamir Detrital Fission-Track Constrains from the Tajik Basin.

Liesa, C.L., Soria, A.R., Meléndez, N., Meléndez, A., 2006. Extensional fault control on the sedimentation patterns in a continental rift basin: El Castellar Formation, Galve sub-basin, Spain. J. Geol. Soc. 163 (3), 487–498. https://doi.org/10.1144/0016-764904-169.

Malusà, M.G., Fitzgerald, P.G., 2019. Application of thermochronology to geologic problems: Bedrock and detrital approaches. In: Fission-Track Thermochronology and its Application to Geology. Springer International Publishing, pp. 191–209.

Mann, U., Stein, R., 1997. Organic facies variations, source rock potential, and sea level changes in cretaceous black shales of the Quebrada Ocal, Upper Magdalena Valley, Colombia. AAPG Bull. 81 (4), 556–576.

Martín-Rincón, C.L., Terraza-Melo, R., Rojas Parra, N.R., Martínez Aparicio, G.A., Rojas Jiménez, S., Hernández González, J.S., 2022. The Upper cretaceous (Santonian-Maastrichtian) phosphate deposits in the west of the Neiva subbasin, Upper Magdalena Valley, Colombia. Bol. Geol. 49 (2), 75–96. https://doi.org/10.32685/0120-1425/bol.geol.49.2.2022.621.

McPherson, J.G., 1979. Calcrete (caliche) palaeosols in fluvial redbeds of the Aztec siltstone (upper Devonian), Southern Victoria Land, Antarctica. Sediment. Geol. 22 (3–4), 267–285. https://doi.org/10.1016/0037-0738(79)90056-3.

Mejia, P., Dilcher, D., Jaramillo, C., Fortini, L., 2012. Palynological composition of a lower cretaceous South American tropical sequence: Climatic implications and diversity comparisons with other latitudes. Am. J. Bot. 99, 1819–1827.

Mesa, A., 2002. Diagénesis de la Formación Caballos, Subcuenca de Girardot : Implicaciones en la Calidad del Reservorio. Asociación Colombiana de Geologos y Geofisicos Del Petroleo, pp. 1–14.

Miall, A.D., 1977. A review of the braided-river depositional environment. Earth Sci. Rev. 13 (1), 1–62. https://doi.org/10.1016/0012-8252(77)90055-1.

Miall, A.D., 1985. Architectural-element analysis: A new method of facies analysis applied to fluvial deposits. Earth Sci. Rev. 22 (4), 261–308. https://doi.org/10.1016/0012-8252(85)90001-7.

Miller, K.G., Sugarman, P.J., Browning, J.V., Kominz, M.A., Olsson, R.K., Feigenson, M. D., Hernández, J.C., 2004. Upper cretaceous sequences and sea-level history, New Jersey Coastal Plain. Geol. Soc. Am. Bull. 116 (3), 368. https://doi.org/10.1130/b25279.1.

Mojica, J., Macía, C., 1981. Características estratigráficas y edad de la Formación Yaví, Mesozoico de la región entre Prado y Dolores, Tolima, Colombia. Geolo. Colombiana 12, 7–31.

Mojica, J., Villarroel, C., 1990. Sobre la distribución y facies del Paleozoico Inferior sedimentario en el extremo NW de Sudamérica. Geolo. Colombiana 17, 219–226.

Montes, C., Cardona, A., Jaramillo, C., Pardo, A., Silva, J.C., Valencia, V., Ayala, C., Pérez-Angel, L.C., Rodriguez-Parra, L.A., Ramirez, V., Niño, H., 2015. Middle Miocene closure of the Central American Seaway. Science (New York, N.Y.) vol. 348 (6231), 226–229. https://doi.org/10.1126/science.aaa2815.

Montes, C., Rodriguez-Corcho, A.F., Bayona, G., Hoyos, N., Zapata, S., Cardona, A., 2019. Continental margin response to multiple arc-continent collisions: the northern Andes-Caribbean margin. Earth Sci. Rev. 198 (102903), 102903 https://doi.org/10.1016/j.earscirev.2019.102903.

Mora, A., Parra, M., Strecker, M.R., Kammer, A., Dimaté, C., Rodríguez, F., 2006. Cenozoic contractional reactivation of Mesozoic extensional structures in the Eastern Cordillera of Colombia. Tectonics 25 (2). https://doi.org/10.1029/2005tc001854.

Mora, A., Horton, B.K., Mesa, A., Rubiano, J., Ketcham, R.A., Parra, M., Blanco, V., Garcia, D., Stockli, D.F., 2009. Migration of Cenozoic deformation in the Eastern Cordillera of Colombia interpreted from fission track results and structural relationships: Implications for petroleum systems. AAPG Bull. 94 (10), 1543–1580. https://doi.org/10.1306/01051009111.

Mora, A., Reyes-Harker, A., Rodriguez, G., Tesón, E., Ramirez-Arias, J.C., Parra, M., Caballero, V., Mora, J.P., Quintero, I., Valencia, V., Ibañez, M., Horton, B.K., Stockli, D.F., 2013. Inversion tectonics under increasing rates of shortening and sedimentation: Cenozoic example from the Eastern Cordillera of Colombia. Geol. Soc. Spec. Publ. 377 (1), 411–442. https://doi.org/10.1144/sp377.6.

Mora, A., Villagómez, D., Parra, M., Caballero, V., Spikings, R., Horton, B., Mora-Bohorquez, J.A., Ketcham, R., Arias-Martinez, J., 2020. Late cretaceous to Cenozoic Uplift of the Northern Andes: Paleogeographic Implications. Geol. Colombia 89–121.

Mora-Bohorquez, J.A., Mantilla, M., De Freitas, M., 2010. Cretaceous paleogeography and sedimentation in the Upper Magdalena and Putumayo basins, southwestern Colombia. In: Search and Discovery Article #50246. Adapted from Expanded Abstract for Oral Presentation at AAPG International Conference and Exhibition.

Moreno-López, M.C., Escalona, A., 2015. Precambrian–Pleistocene tectno-stratigraphic evolution of the southern Llanos basin, Colombia. AAPG Bull. 99 (08), 1473–1501. https://doi.org/10.1306/11111413138.

Naranjo, A., Horner, J., Jahoda, R., Diamond, L.W., Castro, A., Uribe, A., Perez, C., Paz, H., Mejia, C., Weil, J., 2018. La colosa au porphyry deposit, Colombia: Mineralization styles, structural controls, and age constraints. Econ. Geol. Bull. Soc. Econ. Geol. 113 (3), 553–578. https://doi.org/10.5382/econgeo.2018.4562.

Nichols, G., 2009. Sedimentology and Stratigraphy. John Wiley & Sons.

Nie, J., Horton, B.K., Saylor, J.E., Mora, A., Mange, M., Garzione, C.N., Basu, A., Moreno, C.J., Caballero, V., Parra, M., 2012. Integrated provenance analysis of a convergent retroarc foreland system: U–Pb ages, heavy minerals, Nd isotopes, and sandstone compositions of the Middle Magdalena Valley basin, northern Andes, Colombia. Earth Sci. Rev. 110 (1–4), 111–126. https://doi.org/10.1016/j.earscirev.2011.11.002.

Nivia, A., Marriner, G.F., Kerr, A.C., Tarney, J., 2006. The Quebradagrande complex: A lower cretaceous ensialic marginal basin in the Central Cordillera of the Colombian Andes. J. S. Am. Earth Sci. 21 (4), 423–436. https://doi.org/10.1016/j.jsames.2006.07.002.

Noel, J.P., Robert, D.W., 2010. Facies Models 4. Geological Association of Canada.

Ochoa, D., Hoorn, C., Jaramillo, C., Bayona, G., Parra, M., De la Parra, F., 2012. The final phase of tropical lowland conditions in the axial zone of the Eastern Cordillera of Colombia: evidence from three palynological records. J. S. Am. Earth Sci. 39, 157–169. https://doi.org/10.1016/j.jsames.2012.04.010.

Ordóñez-Carmona, O., Restrepo Álvarez, J.J., Pimentel, M.M., 2006. Geochronological and isotopical review of pre-Devonian crustal basement of the Colombian Andes. J. S. Am. Earth Sci. 21 (4), 372–382. https://doi.org/10.1016/j.jsames.2006.07.005.

Ortiz, J., Jaramillo, C., 2018. SDAR. The Smithsonian Institution. https://doi.org/10.25573/DATA.13118426.V2.

Pachón-Parra, L.F., Mann, P., Cardozo, N., 2020. Regional subsurface mapping and 3D flexural modeling of the obliquely converging Putumayo foreland basin, southern Colombia. Interpretation 8 (4). https://doi.org/10.1190/int-2020-0021.1. ST15–ST48.

Parra, M., Mora, A., Sobel, E.R., Strecker, M.R., González, R., 2009. Episodic orogenic front migration in the northern Andes: Constraints from low-temperature thermochronology in the Eastern Cordillera, Colombia. Tectonics 28 (4). https://doi.org/10.1029/2008tc002423.

Parra, M., Mora, A., Lopez, C., Ernesto Rojas, L., Horton, B.K., 2012. Detecting earliest shortening and deformation advance in thrust belt hinterlands: example from the Colombian Andes. Geology 40 (2), 175–178. https://doi.org/10.1130/g32519.1.

Parra, M., Echeverri, S., Patiño, A.M., Ramírez, J.C., Mora, A., Sobel, E.R., Almendral, A., Pardo-Trujillo, A., 2020. Cenozoic evolution of the Sierra Nevada de Santa Marta, Colombia. In: Gómez, J., Mateus-Zabala, D. (Eds.), The Geology of Colombia, Volume 3 Paleogene – Neogene. Servicio Geológico Colombiano, 37. Publicaciones Geológicas Especiales, Bogotá, pp. 185–213. https://doi.org/10.32685/pub.esp.37.2019.07.

Pastor-Chacón, A., Reyes-Abril, J., Aguilera, R., Velandia, F., Piraquive, A., Sarmiento, G., Isaacson, P., 2023. The Devonian system in northwestern Gondwana: Focus on Colombia. Earth Sci. Rev. 243 (104490), 104490 https://doi.org/10.1016/j.earscirev.2023.104490.

Patarroyo, P., 2011. Upper cretaceous Ammonite Succession (Cenomanian-Coniacian) Related to the Upper Hondita and Loma Gorda Formations along the Bambucá Creek, Aipe-Huila (Colombia, Sa) Abstract. Boletín de Geol. 33 (1), 69–92.

Pérez-Consuegra, N., Ott, R.F., Hoke, G.D., Galve, J.P., Pérez-Peña, V., Mora, A., 2021. Neogene variations in slab geometry drive topographic change and drainage reorganization in the Northern Andes of Colombia. Glob. Planet. Chang. 206 (103641), 103641 https://doi.org/10.1016/j.gloplacha.2021.103641.

Pfiffner, O.A., 2017. Thick-skinned and thin-skinned tectonics: A global perspective. Geosciences 7 (3), 71. https://doi.org/10.3390/geosciences7030071.

Phillips, T.B., Fazlikhani, H., Gawthorpe, R.L., Fossen, H., Jackson, C.A.-L., Bell, R.E., Faleide, J.I., Rotevatn, A., 2019. The influence of structural inheritance and multiphase extension on rift development, the NorthernNorth Sea. Tectonics 38 (12), 4099–4126. https://doi.org/10.1029/2019tc005756.

Prössl, K., Vergara, L., 1993. Upper Magdalena Valley, Colombia. An integrated sedimentological and palynological study. Neues Jb. Geol. Paläontol. Abh. 188 (2), 213–240.

Rahn, M., Wang, H., Dunkl, I., 2019. A natural long-term annealing experiment for the zircon fission track system in the Songpan-Garzê flysch, China. Terra Nova 31 (3), 295–305. https://doi.org/10.1111/ter.12399.
Ramon, J.C., Rosero, A., 2006. Multiphase structural evolution of the western margin of the Girardot subbasin, Upper Magdalena Valley, Colombia. J. S. Am. Earth Sci. 21 (4), 493–509. https://doi.org/10.1016/j.jsames.2006.07.012.
Ramos, V.A., 2010. The Grenville-age basement of the Andes. J. S. Am. Earth Sci. 29 (1), 77–91. https://doi.org/10.1016/j.jsames.2009.09.004.
Randon, C., Caridroit, M., 2008. Age and origin of Mississippian lydites: examples from the Pyrénées, southern France. Geol. J. 43 (2–3), 261–278.
Rangel, A., Parra, P., Niño, C., 2000. The La Luna formation: chemostratigraphy and organic facies in the Middle Magdalena Basin. Org. Geochem. 31 (12), 1267–1284. https://doi.org/10.1016/s0146-6380(00)00127-3.
Reimann-Zumsprekel, C.R., Bahlburg, H., Carlotto, V., Boekhout, F., Berndt, J., Lopez, S., 2015. Multi-method provenance model for early Paleozoic sedimentary basins of southern Peru and northern Bolivia (13°–18°S). J. S. Am. Earth Sci. 64, 94–115. https://doi.org/10.1016/j.jsames.2015.08.013.
Reiners, P.W., 2005. Zircon (U-Th)/he thermochronometry. Rev. Mineral. Geochem. 58 (1), 151–179. https://doi.org/10.2138/rmg.2005.58.6.
Reiners, P.W., Brandon, M.T., 2006. Using thermochronology to understand orogenic erosion. Annu. Rev. Earth Planet. Sci. 34 (1), 419–466. https://doi.org/10.1146/annurev.earth.34.031405.125202.
Restrepo, M., Bustamante, C., Cardona, A., Beltrán-Triviño, A., Bustamante, A., Chavarría, L., Valencia, V.A., 2021. Tectonic implications of the jurassic magmatism and the metamorphic record at the southern Colombian Andes. J. S. Am. Earth Sci. 111 (103439), 103439 https://doi.org/10.1016/j.jsames.2021.103439.
Reyes-Harker, A., Ruiz-Valdivieso, C.F., Mora, A., Ramírez-Arias, J.C., Rodriguez, G., de la Parra, F., Caballero, V., Parra, M., Moreno, N., Horton, B.K., Saylor, J.E., Silva, A., Valencia, V., Stockli, D., Blanco, V., 2015. Hyperspectral imaging for the determination of bitumen content in Athabasca oil sands core samples. AAPG Bull. 99 (08), 1407–1453. https://doi.org/10.1306/06181411110.
Rodríguez, G., Arango, M.I., Zapata, G.G., Bermúdez, J.G., 2016. Catálogo de unidades litoestratigráficas de Colombia - Formación Saldaña - Cordilleras Central y Oriental Tolima, Huila, Cauca y Putumayo. Catálogos Estratigráficos Servicio Geológico Colombiano, April, p. 91.
Rodríguez, G., Arango, M.I., Zapata, G., Bermúdez, J.G., 2018. Petrotectonic characteristics, geochemistry, and U-Pb geochronology of Jurassic plutons in the Upper Magdalena Valley-Colombia: Implications on the evolution of magmatic arcs in the NW Andes. J. S. Am. Earth Sci. 81, 10–30. https://doi.org/10.1016/j.jsames.2017.10.012.
Rodríguez-García, G., Correa-Martínez, A.M., Zapata-García, G., Arango-Mejía, M.I., Obando-Erazo, G., Zapata-Villada, J.P., Bermúdez, J.G., 2020. Diverse Jurassic magmatic arcs of the Colombian Andes: Constraints from petrography, geochronology, and geochemistry. In: Gómez, J., Pinilla-Pachon, A.O. (Eds.), The Geology of Colombia, Volume 2 Mesozoic. Servicio Geológico Colombiano, 36. Publicaciones Geológicas Especiales, Bogotá, p. 54. https://doi.org/10.32685/pub.esp.36.2019.04.
Roncancio, J., Martinez, M., 2011. Geology and hydrocarbon potential of the Upper Magdalena Basin. In: Cediel, J., Colmenares, F. (Eds.), Petroleum Geology of Colombia, volume 14. Upper Magdalena Basin. Agencia Nacional de Hidrocarburos (ANH). https://www.anh.gov.co/es/hidrocarburos/informaci%C3%B3n-geol%C3%B3gica-y-geof%C3%ADsica/estudios-integrados-y-modelamientos/petroleum-geology-of-colombia/.
Roure, F., 2008. Foreland and Hinterland basins: what controls their evolution? Swiss J. Geosci. 101 (S1), 5–29. https://doi.org/10.1007/s00015-008-1285-x.
Rubatto, D., 2002. Zircon trace element geochemistry: partitioning with garnet and the link between U–Pb ages and metamorphism. Chem. Geol. 184 (1–2), 123–138. https://doi.org/10.1016/s0009-2541(01)00355-2.
Rubiano-Ortiz, J.L., 1989. Petrography and Stratigraphy of the Villeta Group, Cordillera Oriental, Colombia, South America (Doctoral dissertation,. University of South Carolina.
Saeid, E., Bakioglu, K.B., Kellogg, J., Leier, A., Martinez, J.A., Guerrero, E., 2017. Garzón Massif basement tectonics: Structural control on evolution of petroleum systems in upper Magdalena and Putumayo basins, Colombia. Mar. Pet. Geol. 88, 381–401. https://doi.org/10.1016/j.marpetgeo.2017.08.035.
Sarmiento-Rojas, Luis Fernando, 2019. Cretaceous stratigraphy and Paleo-facies maps of northwestern South America. In: Geology and Tectonics of Northwestern South America. Springer International Publishing, pp. 673–747.
Sarmiento-Rojas, L.F., Van Wess, J.D., Cloetingh, S., 2006. Mesozoic transtensional basin history of the Eastern Cordillera, Colombian Andes: Inferences from tectonic models. J. S. Am. Earth Sci. 21 (4), 383–411. https://doi.org/10.1016/j.jsames.2006.07.003.
Schneider, S., Hornung, J., Hinderer, M., 2017. Evolution of the northern Albertine Rift reflected in the provenance of synrift sediments (Nkondo-Kaiso area, Uganda). J. African Earth Sci. (Oxford, England: 1994) 131, 183–197. https://doi.org/10.1016/j.jafrearsci.2017.04.012.
Scisciani, V., Patruno, S., Tavarnelli, E., Calamita, F., Pace, P., Iacopini, D., 2019. Multi-phase reactivations and inversions of Paleozoic–Mesozoic extensional basins during the Wilson cycle: case studies from the North Sea (UK) and the Northern Apennines (Italy). Geol. Soc. Spec. Publ. 470 (1), 205–243. https://doi.org/10.1144/sp470-2017-232.
Shanley, K.W., McCABE, P.J., Hettinger, R.D., 1992. Tidal influence in cretaceous fluvial strata from Utah, USA: a key to sequence stratigraphic interpretation. Sedimentology 39 (5), 905–930. https://doi.org/10.1111/j.1365-3091.1992.tb02159.x.
Shiers, M.N., Mountney, N.P., Hodgson, D.M., Colombera, L., 2018. Controls on the depositional architecture of fluvial point-bar elements in a coastal-plain succession. In: Fluvial Meanders and their Sedimentary Products in the Rock Record. Wiley, pp. 15–46. https://doi.org/10.1002/9781119424437.ch2.
Siks, B.C., Horton, B.K., 2011. Growth and fragmentation of the Andean foreland basin during eastward advance of fold-thrust deformation, Puna plateau and Eastern Cordillera, northern Argentina: Fragmentation of Andean Foreland Basin. Tectonics 30 (6). https://doi.org/10.1029/2011tc002944.
Siravo, G., Faccenna, C., Gérault, M., Becker, T.W., Fellin, M.G., Herman, F., Molin, P., 2019. Slab flattening and the rise of the Eastern Cordillera, Colombia. Earth Planet. Sci. Lett. 512, 100–110. https://doi.org/10.1016/j.epsl.2019.02.002.
Smyth, H.R., Hall, R., Nichols, G.J., 2008. Significant volcanic contribution to some quartz-rich sandstones, east java, Indonesia. J. Sediment. Res. 78 (5), 335–356. https://doi.org/10.2110/jsr.2008.039.
Sneider, J., 1988. Depositional Environment of the Caballos Formation, San Francisco field, Neiva sub-basin, Upper Magdalena Valley. Issue Texas A&M University, Colombia.
Spikings, R., Cochrane, R., Villagomez, D., Van der Lelij, R., Vallejo, C., Winkler, W., Beate, B., 2015. The geological history of northwestern South America: from Pangaea to the early collision of the Caribbean large Igneous Province (290–75Ma). Gondwana Res.: Int. Geosci. J. 27 (1), 95–139. https://doi.org/10.1016/j.gr.2014.06.004.
Stibane, F., Forero, A., 1969. Vista de Los afloramientos del Paleozoico en La Jagua (Huila) y Río Nevado (Santander del Sur). Pdf. Geolo. Colombiana 9 (3), 31–66.
Stojadinovic, U., Matenco, L., Andriessen, P., Toljić, M., Rundić, L., Ducea, M.N., 2017. Structure and provenance of Late Cretaceous–Miocene sediments located near the NE Dinarides margin: Inferences from kinematics of orogenic building and subsequent extensional collapse. Tectonophysics 710–711, 184–204. https://doi.org/10.1016/j.tecto.2016.12.021.
Strecker, M.R., Hilley, G.E., Bookhagen, B., Sobel, E.R., 2011. Structural, geomorphic, and depositional characteristics of contiguous and broken foreland basins: Examples from the Eastern flanks of the Central Andes in Bolivia and NW Argentina. In: Tectonics of Sedimentary Basins. Wiley, pp. 508–521. https://doi.org/10.1002/9781444347166.ch25.
Tagami, T., O'Sullivan, P.B., 2005. Fundamentals of fission-track thermochronology. Rev. Mineral. Geochem. 58 (1992), 19–47. https://doi.org/10.2138/rmg.2005.58.2.
Tagami, T., Galbraith, R.F., Yamada, R., Laslett, G.M., 1998. Revised annealing kinetics of fission tracks in zircon and geological implications. In: Advances in Fission-Track Geochronology. Springer, Netherlands, pp. 99–112.
Terraza-Melo, R., 2012. Stratigraphy and deposit environments of the arenisca de chiquinquira around its type locality; Estratigrafia y ambientes de deposito de la arenisca de chiquinquira en los alrededores de la localidad tipo. Bolet. de Geol. Univ. Ind. Santand. 34. https://www.osti.gov/etdeweb/biblio/22108883.
Turner, B.R., Tester, G.N., 2006. The Table Rocks Sandstone: A fluvial, friction-dominated lobate mouth bar sandbody in the Westphalian B Coal measures, NE England. Sediment. Geol. 190 (1–4), 97–119. https://doi.org/10.1016/j.sedgeo.2006.05.007.
Valencia-Gómez, J.C., Cardona, A., Bayona, G., Valencia, V., Zapata, S., 2020. Análisis de procedencia del registro sin-orogénico Maastrichtiano de la Formación Cimarrona, flanco occidental de la Cordillera Oriental colombiana. Rev. Boletín de Geol. 42 (3), 171–204. https://doi.org/10.18273/revbol.v42n3-2020008.
Van Der Wiel, A.M., 1991. Uplift and Volcanism of the SE Colombian Andes in Relation to Neogene Sedimentation in the Upper Magdalena Valley.
Vásquez, M., Altenberger, U., Romer, R.L., Sudo, M., Moreno-Murillo, J.M., 2010. Magmatic evolution of the Andean Eastern Cordillera of Colombia during the cretaceous: Influence of previous tectonic processes. J. S. Am. Earth Sci. 29 (2), 171–186. https://doi.org/10.1016/j.jsames.2009.02.003.
Veloza, G., Mora, A., De Freitas, A., Mantilla, M., 2008. Dislocación De Facies En El Tope De La Secuencia Cretácica De La Subcuenca De Neiva, Valle Superior Del Magdalena Y Sus Implicaciones En El Modelo Estratigráfico Secuencial Colombiano. Bolet. de Geol. 30 (1), 29–44.
Vergara, L.S., 1997. Stratigraphy, foraminiferal assemblages and paleoenvironments in the late cretaceous of the Upper Magdalena Valley, Colombia (part I). J. S. Am. Earth Sci. 10 (2), 111–132. https://doi.org/10.1016/s0895-9811(97)00010-2.
Vermeesch, P., 2012. On the visualisation of detrital age distributions. Chem. Geol. 312–313, 190–194. https://doi.org/10.1016/j.chemgeo.2012.04.021.
Vermeesch, P., 2018. IsoplotR: A free and open toolbox for geochronology. Geosci. Front. 9 (5), 1479–1493. https://doi.org/10.1016/j.gsf.2018.04.001.
Villagómez, D., Spikings, R., 2013. Thermochronology and tectonics of the Central and Western Cordilleras of Colombia: Early Cretaceous–Tertiary evolution of the Northern Andes. Lithos 160–161, 228–249. https://doi.org/10.1016/j.lithos.2012.12.008.
Villagómez, D., Spikings, R., Magna, T., Kammer, A., Winkler, W., Beltrán, A., 2011. Geochronology, geochemistry and tectonic evolution of the Western and Central cordilleras of Colombia. Lithos 125 (3–4), 875–896. https://doi.org/10.1016/j.lithos.2011.05.003.
Villamil, T., 1999. Campanian–Miocene tectonostratigraphy, depocenter evolution and basin development of Colombia and western Venezuela. Palaeogeogr. Palaeoclimatol. Palaeoecol. 153 (1–4), 239–275. https://doi.org/10.1016/s0031-0182(99)00075-9.
Villamizar-Escalante, N., Bernet, M., Urueña-Suárez, C., Hernández-González, J.S., Terraza-Melo, R., Roncancio, J., Muñoz-Rocha, J.A., Peña-Urueña, M.L., Amaya, S., Piraquive, A., 2021. Thermal history of the southern Central Cordillera and its exhumation record in the Cenozoic deposits of the Upper Magdalena Valley, Colombia. J. S. Am. Earth Sci. 107 (103105), 103105 https://doi.org/10.1016/j.jsames.2020.103105.
Vinasco, C.J., Cordani, U.G., González, H., Weber, M., Pelaez, C., 2006. Geochronological, isotopic, and geochemical data from Permo-Triassic granitic

gneisses and granitoids of the Colombian Central Andes. J. S. Am. Earth Sci. 21 (4), 355–371. https://doi.org/10.1016/j.jsames.2006.07.007.
Voigt, S., Lucas, S.G., Krainer, K., 2013. Coastal-plain origin of trace-fossil bearing red beds in the early Permian of Southern New Mexico, USA. Palaeogeogr. Palaeoclimatol. Palaeoecol. 369, 323–334.
Wagner, G., Van den Haute, P., 1992. Fission-Track Dating: Solid Earth Sciences Library. Kluwer Academic Publishers, Amsterdam.
Wagner, G., Gleadow, A., Fitzgerald, P., 1989. The significance of the partial annealing zone in apatite fission-track analysis: projected track length measurements and uplift chronology of the transantarctic mountains. Chem. Geol.: Isotope Geosci. Sect. 79 (4), 295–305. https://doi.org/10.1016/0168-9622(89)90035-3.
Wagner, L.S., Jaramillo, J.S., Ramírez-Hoyos, L.F., Monsalve, G., Cardona, A., Becker, T. W., 2017. Transient slab flattening beneath Colombia. Geophys. Res. Lett. 44 (13), 6616–6623. https://doi.org/10.1002/2017gl073981.
Yamada, R., Murakami, M., Tagami, T., 2007. Statistical modelling of annealing kinetics of fission tracks in zircon. Reassess. Laborat. Experim. Chem. Geolo. 236 (1–2), 75–91. https://doi.org/10.1016/j.chemgeo.2006.09.002.
Zapata, Sebastian, Cardona, A., Jaramillo, C., Valencia, V., Vervoort, J., 2016. U-Pb LA-ICP-MS Geochronology and Geochemistry of Jurassic Volcanic and Plutonic Rocks from the Putumayo Region (Southern Colombia): Tectonic setting and Regional Correlations. Rev. Boletín de Geol. 38 (2), 21–38. https://doi.org/10.18273/revbol.v38n2-2016001.
Zapata, S., Cardona, A., Jaramillo, J.S., Patiño, A., Valencia, V., León, S., Mejía, D., Pardo-Trujillo, A., Castañeda, J.P., 2019a. Cretaceous extensional and contractional tectonics in the Northwestern Andes, prior to the collision with the Caribbean oceanic plateau. Gondwana Res.: Int. Geosci. J. 66, 207–226. https://doi.org/10.1016/j.gr.2018.10.008.
Zapata, S., Sobel, E.R., Papa, C., Jelinek, A.R., Glodny, J., 2019b. Using a paleosurface to constrain low-temperature thermochronological data: Tectonic evolution of the Cuevas range, Central Andes. Tectonics 38 (11), 3939–3958. https://doi.org/10.1029/2019tc005887.
Zapata, S., Patiño, A., Cardona, A., Parra, M., Valencia, V., Reiners, P., Oboh-Ikuenobe, F., Genezini, F., 2020. Bedrock and detrital zircon thermochronology to unravel exhumation histories of accreted tectonic blocks: An example from the Western Colombian Andes. J. S. Am. Earth Sci. 103 (102715), 102715 https://doi.org/10.1016/j.jsames.2020.102715.
Zapata, S., Zapata-Henao, M., Cardona, A., Jaramillo, C., Silvestro, D., Oboh-Ikuenobe, F., 2021. Long-term topographic growth and decay constrained by 3D thermo-kinematic modeling: Tectonic evolution of the Antioquia Altiplano, Northern Andes. Glob. Planet. Chang. 203 (103553), 103553 https://doi.org/10.1016/j.gloplacha.2021.103553.
Zapata, S., Calderon-Diaz, L., Jaramillo, C., Oboh-Ikuenobe, F., Piedrahita, J.C., Rodríguez-Cuevas, M., Cardona, A., Sobel, E.R., Parra, M., Valencia, V., Patiño, A., Jaramillo-Rios, J.S., Flores, M., Glodny, J., 2023. Drainage and sedimentary response of the Northern Andes and the Pebas system to Miocene strike-slip tectonics: A source to sink study of the Magdalena Basin. Basin Res. https://doi.org/10.1111/bre.12769.
Zapata-Villada, J.P., Cardona, A., Serna, S., Rodríguez, G., 2021. Late cretaceous to Paleocene magmatic record of the transition between collision and subduction in the Western and Central Cordillera of northern Colombia. J. S. Am. Earth Sci. 112, 103557.
Zhou, R., Schoenbohm, L.M., Sobel, E.R., Davis, D.W., Glodny, J., 2017. New constraints on orogenic models of the southern Central Andean Plateau: Cenozoic basin evolution and bedrock exhumation. Geol. Soc. Am. Bull. 129 (1–2), 152–170. https://doi.org/10.1130/b31384.1.